ENGINEERING OF BIOMATERIALS

INŻYNIERIA BIOMATERIAŁÓW

JOURNAL OF POLISH SOCIETY FOR BIOMATERIALS AND FACULTY OF MATERIALS SCIENCE AND CERAMICS AGH-UST

CZASOPISMO POLSKIEGO STOWARZYSZENIA BIOMATERIAŁÓW I WYDZIAŁU INŻYNIERII MATERIAŁOWEJ I CERAMIKI AGH

Number 150
Numer 150
Volume XXII
Rok XXII

APRIL 2019
KWIECIEŃ 2019

ISSN 1429-7248

PUBLISHER:
WYDAWCA:

Polish Society for Biomaterials in Krakow
Polskie Stowarzyszenie Biomateriałów w Krakowie

ADDRESS OF EDITORIAL OFFICE:
ADRES REDAKCJI:

AGH-UST
30/A3, Mickiewicz Av.
30-059 Krakow, Poland
Akademia Górniczo-Hutnicza
al. Mickiewicza 30/A-3
30-059 Kraków

Issue: 250 copies
Nakład: 250 egz.

Scientific Publishing House AKAPIT
Wydawnictwo Naukowe AKAPIT
e-mail: wn@akapit.krakow.pl

ENGINEERING OF BIOMATERIALS

EDITORIAL BOARD
KOMITET REDAKCYJNY

INTERNATIONAL EDITORIAL BOARD
MIĘDZYNARODOWY KOMITET REDAKCYJNY

ENGINEERING OF BIOMATERIALS

Wskazówki dla autorów

1. Prace do opublikowania w kwartalniku „Engineering of Biomaterials / Inżynieria Biomateriałów" przyjmowane będą wyłącznie w języku angielskim. Możliwe jest również dołączenie dodatkowo polskiej wersji językowej.
2. Wszystkie nadsyłane artykuły są recenzowane.
3. Materiały do druku prosimy przysyłać na adres e-mail: kabe@agh.edu.pl.
4. Struktura artykułu:
• TYTUŁ • Autorzy i instytucje • Streszczenie (200-250 słów) • Słowa kluczowe (4-6) • Wprowadzenie • Materiały i metody • Wyniki i dyskusja • Wnioski • Podziękowania • Piśmiennictwo
5. Autorzy przesyłają pełną wersję artykułu, łącznie z ilustracjami, tabelami, podpisami i literaturą w jednym pliku. Artykuł w tej formie przesyłany jest do recenzentów. Dodatkowo autorzy proszeni są o przesłanie materiałów ilustracyjnych (rysunki, schematy, fotografie, wykresy) w oddzielnych plikach (format np. .jpg, .gif., .tiff, .bmp). Rozdzielczość rysunków min. 300 dpi. Wszystkie rysunki i wykresy powinny być czarno-białe lub w odcieniach szarości i ponumerowane cyframi arabskimi. W tekście należy umieścić odnośniki do rysunków i tabel. W przypadku artykułów dwujęzycznych w tabelach i na wykresach należy umieścić opisy polskie i angielskie.
6. Na końcu artykułu należy podać wykaz piśmiennictwa w kolejności cytowania w tekście i kolejno ponumerowany.
7. Redakcja zastrzega sobie prawo wprowadzenia do opracowań autorskich zmian terminologicznych, poprawek redakcyjnych, stylistycznych, w celu dostosowania artykułu do norm przyjętych w naszym czasopiśmie. Zmiany i uzupełnienia merytoryczne będą dokonywane w uzgodnieniu z autorem.
8. Opinia lub uwagi recenzentów będą przekazywane Autorowi do ustosunkowania się. Nie dostarczenie poprawionego artykułu w terminie oznacza rezygnację Autora z publikacji pracy w naszym czasopiśmie.
9. Za publikację artykułów redakcja nie płaci honorarium autorskiego.
10. Adres redakcji:

Czasopismo
„Engineering of Biomaterials / Inżynieria Biomateriałów"
Akademia Górniczo-Hutnicza im. St. Staszica
Wydział Inżynierii Materiałowej i Ceramiki
al. Mickiewicza 30/A-3, 30-059 Kraków
tel. (48) 12 617 25 03, 12 617 25 61
tel./fax: (48) 12 617 45 41
e-mail: chlopek@agh.edu.pl, kabe@agh.edu.pl

Szczegółowe informacje dotyczące przygotowania manuskryptu oraz procedury recenzowania dostępne są na stronie internetowej czasopisma:
www.biomat.krakow.pl

Warunki prenumeraty

Zamówienie na prenumeratę prosimy przesyłać na adres:
mgr inż. Augustyn Powroźnik
apowroz@agh.edu.pl, tel/fax: (48) 12 617 45 41
Cena pojedynczego numeru wynosi 20 PLN
Konto: Polskie Stowarzyszenie Biomateriałów
30-059 Kraków, al. Mickiewicza 30/A-3
ING Bank Śląski S.A. O/Kraków
nr rachunku 63 1050 1445 1000 0012 0085 6001

Prenumerata obejmuje 4 numery regularne i nie obejmuje numeru specjalnego (materiały konferencyjne).

Instructions for authors

1. Papers for publication in quarterly journal „Engineering of Biomaterials / Inżynieria Biomateriałów" should be written in English.
2. All articles are reviewed.
3. Manuscripts should be submitted to editorial office by e-mail to kabe@agh.edu.pl.
4. A manuscript should be organized in the following order:
• TITLE • Authors and affiliations • Abstract (200-250 words) • Keywords (4-6) • Introduction • Materials and Methods • Results and Discussions • Conclusions • Acknowledgements • References
5. All illustrations, figures, tables, graphs etc. preferably in black and white or grey scale should be additionally sent as separate electronic files (format .jpg, .gif., .tiff, .bmp). High-resolution figures are required for publication, at least 300 dpi. All figures must be numbered in the order in which they appear in the paper and captioned below. They should be referenced in the text. The captions of all figures should be submitted on a separate sheet.
6. References should be listed at the end of the article. Number the references consecutively in the order in which they are first mentioned in the text.
7. The Editors reserve the right to improve manuscripts on grammar and style and to modify the manuscripts to fit in with the style of the journal. If extensive alterations are required, the manuscript will be returned to the authors for revision.
8. Opinion or notes of reviewers will be transferred to the author. If the corrected article will not be supplied on time, it means that the author has resigned from publication of work in our journal.
9. Editorial does not pay author honorarium for publication of article.
10. Address of editorial office:

Journal
„Engineering of Biomaterials / Inżynieria Biomateriałów"
AGH University of Science and Technology
Faculty of Materials Science and Ceramics
30/A-3, Mickiewicz Av., 30-059 Krakow, Poland
tel. (48) 12) 617 25 03, 12 617 25 61
tel./fax: (48) 12 617 45 41
e-mail: chlopek@agh.edu.pl, kabe@agh.edu.pl

Detailed information concerning manuscript preparation and review process are available at the journal's website:
www.biomat.krakow.pl

Subscription terms

Contact:
MSc Augustyn Powroźnik,
e-mail: apowroz@agh.edu.pl
Subscription rates:
Cost of one number: 20 PLN
Payment should be made to:
Polish Society for Biomaterials
30/A3, Mickiewicz Av.
30-059 Krakow, Poland
ING Bank Slaski S.A.
account no. 63 1050 1445 1000 0012 0085 6001

Subscription includes 4 issues and does not include special issue (conference materials).

28th Biomaterials in Medicine and Veterinary Medicine

Annual Conference

10 – 13 October 2019 Rytro, Poland

SAVE THE DATE

10-13

OCTOBER

2019

www.biomat.agh.edu.pl

REGISTER

AND

SUBMIT

AN ABSTRACT

STUDIA PODYPLOMOWE

Biomateriały – Materiały dla Medycyny

2019/2020

Organizator: Akademia Górniczo-Hutnicza im. Stanisława Staszica w Krakowie Wydział Inżynierii Materiałowej i Ceramiki Katedra Biomateriałów i Kompozytów **Kierownik:** prof. dr hab. inż. Elżbieta Pamuła **Sekretarz:** dr inż. Małgorzata Krok-Borkowicz	**Adres:** 30-059 Kraków, Al. Mickiewicza 30 Pawilon A3, p. 208, 210 lub 501 tel. 12 617 44 48, 12 617 23 38, fax. 12 617 33 71 email: epamula@agh.edu.pl; krok@agh.edu.pl https://www.agh.edu.pl/ksztalcenie/oferta-ksztalcenia/studia-podyplomowe-kursy-doksztalcajace-i-szkolenia/biomaterialy-materialy-dla-medycyny/

Charakterystyka:
Tematyka prezentowana w trakcie zajęć obejmuje przegląd wszystkich grup materiałów dla zastosowań medycznych: metalicznych, ceramicznych, polimerowych, węglowych i kompozytowych. Słuchacze zapoznają się z metodami projektowania i wytwarzania biomateriałów a następnie możliwościami analizy ich właściwości mechanicznych, właściwości fizykochemicznych (laboratoria z metod badań: elektronowa mikroskopia skaningowa, mikroskopia sił atomowych, spektroskopia w podczerwieni, badania energii powierzchniowej i zwilżalności) i właściwości biologicznych (badania: *in vitro* i *in vivo*). Omawiane są regulacje prawne i aspekty etyczne związane z badaniami na zwierzętach i badaniami klinicznymi (norma EU ISO 10993). Słuchacze zapoznają się z najnowszymi osiągnięciami w zakresie nowoczesnych nośników leków, medycyny regeneracyjnej i inżynierii tkankowej.

Sylwetka absolwenta:
Studia adresowane są do absolwentów uczelni technicznych (inżynieria materiałowa, technologia chemiczna), przyrodniczych (chemia, biologia, biotechnologia) a także medycznych, stomatologicznych, farmaceutycznych i weterynaryjnych, pragnących zdobyć, poszerzyć i ugruntować wiedzę z zakresu inżynierii biomateriałów i nowoczesnych materiałów dla medycyny. Słuchacze zdobywają i/lub pogłębiają wiedzę z zakresu inżynierii biomateriałów. Po zakończeniu studiów wykazują się znajomością budowy, właściwości i sposobu otrzymywania materiałów przeznaczonych dla medycyny. Potrafią analizować wyniki badań i przekładać je na zachowanie się biomateriału w warunkach żywego organizmu. Ponadto słuchacze wprowadzani są w zagadnienia dotyczące wymagań normowych, etycznych i prawnych niezbędnych do wprowadzenia nowego materiału na rynek. Ukończenie studiów pozwala na nabycie umiejętności przygotowywania wniosków do Komisji Etycznych i doboru metod badawczych w zakresie analizy biozgodności materiałów.

Zasady naboru:
Termin zgłoszeń: od 20.09.2019 do 20.10.2019 (liczba miejsc ograniczona - decyduje kolejność zgłoszeń)
Wymagane dokumenty: dyplom ukończenia szkoły wyższej
Osoby przyjmujące zgłoszenia:
prof. dr hab. inż. Elżbieta Pamuła (pawilon A3, p. 208, tel. 12 617 44 48, e-mail: epamula@agh.edu.pl)
dr inż. Małgorzata Krok-Borkowicz (pawilon A3, p. 210, tel. 12 617 23 38, e-mail: krok@agh.edu.pl)

Czas trwania: 2 semestry (od XI 2019 r. do VI 2020 r.) 8 zjazdów (soboty-niedziele) 1 raz w miesiącu	**Opłaty:** 2 600 zł (za dwa semestry)

SPIS TREŚCI
CONTENTS

Wersja papierowa czasopisma „Engineering of Biomaterials / Inżynieria Biomateriałów" jest jego wersją pierwotną
Printed version of „Engineering of Biomaterials / Inżynieria Biomateriałów" is a primary version of the journal

ANALIZA MATERIAŁOZNAWCZA DEIMPLANTOWANEGO ELEMENTU ENDOPROTEZY STAWU BIODROWEGO

Marta Płatek[1]*, Agata Dudek[2], Jarosław Ucieklak[3]

[1] Politechnika Łódzka,
Instytut Inżynierii Materiałowej,
ul. Stefanowskiego 1/15, 90-924 Łódź
[2] Politechnika Częstochowska,
Wydział Inżynierii Produkcji i Technologii Materiałów
Al. Armii Krajowej 19, 42-200 Częstochowa
[3] Szpital Czerniakowski Sp. z o. o.,
ul. Stępińska 19/25, 00-739 Warszawa
*e-mail: mgluszek06@gmail.com

Streszczenie

Pomimo postępu jaki dokonał się w ostatnich latach w zakresie endoprotezoplastyk stawu biodrowego jednym z nierozwiązanych do końca zagadnień pozostaje problem aseptycznych i septycznych obluzowań elementów endoprotez. Dlatego stale trwają poszukiwania rozwiązań pozwalających zminimalizować ryzyko zapaleń okołoprotezowych i aseptycznych obluzowań endoprotez. Przedmiotem badania był trzpień endoprotezy Mittelmeiera usunięty z powodu aseptycznego obluzowania po 16 latach od wszczepienia. Przeprowadzano analizę strukturalną wykorzystując mikroskop świetlny i skaningowy oraz zbadano skład chemiczny materiału, z którego wykonano implant. Dokonano również oceny stopnia degradacji jego powierzchni. Analiza składu chemicznego porównana do pierwotnego składu tego trzpienia ujawniła, iż bezpośredni kontakt implantu z płynami ustrojowymi i żywą tkanką wpływa na zmianę ilościową poszczególnych pierwiastków. Mikroskopia skaningowa elektronowa ujawniła na metalowym trzpieniu liczne wżery, pęknięcia oraz ubytki powstałe na skutek zużycia oraz korozji. Wykonane badania wykazały, że nie tylko implant osadzony w kości oddziałuje na okoliczne tkanki, ale zachodzą zmiany również w obrębie wszczepionego implantu. Bezpośrednią przyczyną obluzowania implantu była osteoliza związana z nagromadzeniem w przestrzeni pomiędzy implantem a kością elementów zużycia korozyjnego i erozyjnego. Na podstawie zebranych danych z Oddziału Chirurgii Urazowo-Ortopedycznej Szpitala Czerniakowskiego Sp. z o.o. w Warszawie wykonano ponadto analizę statystyczną przeprowadzonych endoprotezoplastyk pierwotnych i rewizyjnych oraz występujących powikłań, ze szczególnym uwzględnieniem obluzowań elementów endoprotez, które wymagały operacji rewizyjnych.

Słowa kluczowe: *endoprotezoplastyka stawu biodrowego, trzpień endoprotezy, rewizja, stop Co-Cr-Mo*

[Engineering of Biomaterials 150 (2019) 2-9]

Article presented at conference: IMPLANTS 2019, 28-29 June, Gdansk, Poland.

MATERIAL ANALYSIS OF THE DEIMPLANTED ELEMENT OF HIP JOINT ENDOPROSTHESIS

Marta Płatek[1]*, Agata Dudek[2], Jarosław Ucieklak[3]

[1] Lodz University of Technology,
Institute of Materials Science and Engineering,
ul. Stefanowskiego 1/15, 90-924 Łódź, Poland
[2] Czestochowa University of Technology,
Faculty of Production Engineering
and Materials Technology,
Al. Armii Krajowej 19, 42-200 Częstochowa
[3] Szpital Czerniakowski Sp. z o. o.,
ul. Stępińska 19/25, 00-739 Warszawa, Poland
*e-mail: mgluszek06@gmail.com

Abstract

Despite the progress that has been made in recent years in the field of hip joint endoprostheses, the problem of aseptic and septic loosening of endoprosthetic elements remains one of the unresolved issues. Therefore, the research on solutions to minimize the risk of periprosthetic inflammations and aseptic loosening of endoprostheses is still ongoing. The subject of the study was a stem of the Mittelmeier's endoprosthesis removed due to its aseptic loosening after 16 years of implantation. The structural analysis was carried out using a light and scanning microscope and the chemical composition of the implant material was examined. The analysis of the chemical composition compared to the original composition of the stem revealed that direct contact of the implant with body fluids and living tissue affects the quantitative change of individual elements. Scanning electron microscopy revealed numerous pitting, cracks and losses caused by wear and corrosion on the metal stem. The research carried out showed that not only does the implant inserted in the bone affect the surrounding tissue, but there are also changes within the implanted prosthesis. The direct cause of the implant loosening was osteolysis in the space between the implant and the bone, associated with the accumulation of elements of corrosion and erosion wear. Based on the collected results from the Trauma and Orthopaedic Surgery Department of the Czerniakowski Hospital in Warsaw, a statistical analysis of primary and revision endoprostheses and complications was performed, with particular emphasis on the loosening of the endoprostheses elements that required revision surgeries.

Keywords: *hip joint endoprosthesis, stem of endoprosthesis, revision, Co-Cr-Mo alloy*

[Engineering of Biomaterials 150 (2019) 2-9]

Article presented at conference: IMPLANTS 2019, 28-29 June, Gdansk, Poland.

Wprowadzenie

Jednym z powszechnie stosowanych sposobów leczenia zaawansowanych zmian zwyrodnieniowych jest endoprotezoplastyka, zarówno w przypadku schorzeń pierwotnych, jak również wtórnych - wynikających z zaburzeń mechaniki stawu, chorób dziecięcych czy urazów narządu ruchu. Endoprotezoplastyka stawu biodrowego w ostatnich dziesięcioleciach stała się najczęściej wykonywaną procedurą ortopedyczną. Celem zastosowania protezoplastyki stawów jest uwolnienie pacjentów od dolegliwości bólowych i przywrócenie prawidłowej ruchomości stawu [1-2]. Na przestrzeni kolejnych kilkunastu lat nastąpił dynamiczny, technologiczno-konstrukcyjny rozwój nowych generacji endoprotez stawu biodrowego. Doskonalona jest również technika operacyjna oraz instrumentarium, czyniąc alloplastykę metodą coraz bardziej powtarzalną i bezpieczną, zapewniającą poprawę własności biomechanicznych układu kostno-stawowego [3]. Endoprotezoplastyka stawu biodrowego niezależnie od wskazań do jej wykonania, typu użytego implantu czy też wieku chorego, narażona jest na różnego rodzaju powikłania miejscowe i ogólnoustrojowe. Obluzowania endoprotez postrzegane są jako jedna z głównych przyczyn niepowodzeń tego rodzaju zabiegów [4-7].

Czynnikiem warunkującym uzyskanie dobrego rezultatu wymiany stawu biodrowego jest poprawne ułożenie przestrzenne elementów endoprotezy. Dla zapewnienia trwałości przeprowadzonego zabiegu i wysokiego stopnia ruchomości kończyny dolnej, poszczególne elementy muszą być wszczepione we właściwej anatomicznie pozycji. Zapewnione również musi być odpowiednie napięcie tkanek miękkich [1-2,7].

W latach siedemdziesiątych i osiemdziesiątych XX wieku nastąpił gwałtowny rozwój endoprotezoplastyki cementowej stawu biodrowego [3]. Stopniowo ulepszana była technika cementowania implantów, co przekładało się na uzyskiwanie coraz lepszych wyników. Cement miał spełniać rolę spoiwa pozwalającego dopasować obrys implantu do łoża kostnego oraz unieruchomić go względem kości. Jednak równolegle rozwijane były systemy endoprotez bezcementowych [8-9]. Prowadzone badania pozwoliły ustalić, że w przypadku rozwiązań bezcementowych pierwotne osadzenie trzpienia powinno opierać się na bardziej dokładnym dopasowaniu kształtu trzpienia do kształtu jamy szpikowej kości udowej oraz wyeliminowaniu możliwości jego mikroruchów. Pierwszy warunek zaczęto osiągać dzięki zwiększaniu liczby rozmiarów trzpieni, umożliwiającemu bardziej ścisłe dopasowanie do wielkości jamy szpikowej kości udowej. Drugi dylemat próbowano rozwiązać poprzez różnego rodzaju modyfikacje kształtu trzpieni [10-12]. W 1974 roku Mittelmeier skonstruował endoprotezę, której trzpień pokryty był ożebrowaniem mającym poprawić jego umocowanie w porowatej strukturze kości. Ceramiczna panewka była wkręcana i współpracowała z ceramiczna głową modularną. Była to jedna z pierwszych endoprotez bezcementowych szerzej wprowadzonych do praktyki klinicznej. Pomimo ulepszonych rozwiązań nadal spotyka się pacjentów korzystających z tego modelu endoprotezy [3,10-12].

Z biegiem lat przekonano się, że to początkowe, ścisłe dopasowanie trzpienia endoprotezy do kształtu jamy szpikowej, zapewniające pierwotną stabilizację, wystarcza tylko na pewien czas [9,11-12]. Pod wpływem przenoszonych obciążeń, z upływem czasu pojawiają się mikroruchy trzpienia prowadzące do niszczenia łoża kostnego i w konsekwencji powstania obluzowania implantu. Doprowadziło to do rozwoju koncepcji stabilizacji wtórnej polegającej na osteointegracji wszczepu z tkanką kostną. Aby ten cel osiągnąć zaczęto pokrywać implanty porowatymi powłokami o właściwościach osteokondukcyjnych, stanowiącymi rusztowanie dla komórek osteogennych z otaczającej tkanki kostnej [10-12].

Introduction

One of the most popular methods of treating advanced degenerative changes is endoprostheses, both in primary and secondary diseases - resulting from joint mechanics disorders, childhood diseases or locomotive trauma. In recent decades, the hip joint endoprosthesis has become the most frequently performed orthopaedic procedure. The aim of a joint replacement is to relieve patients of pain and restore proper joint mobility [1-2]. Over the last several years, there has been a dynamic, technological and structural development of new generations of hip joint endoprostheses. The surgical techniques and instruments have also been improved, making alloplasty more and more reproducible and safe, as well as ensuring improvement of biomechanical properties of the osteoarticular system [3]. The hip endoprosthetic surgery, regardless of indications for its performance, the type of an implant used or the patient's age, is exposed to various local and systemic complications. Loosening of endoprostheses is one of the main causes of failure of this type of procedures [4-7].

The proper spatial arrangement of endoprosthetic elements is a factor determining the efficiency of hip joint replacement. In order to ensure the procedure durability and future high mobility of the lower limb, the individual elements must be implanted in an anatomically correct position. Adequate soft tissue tension must also be ensured [1-2,7].

In the 1970-80s, there was a rapid development of cement hip joint endoprostheses [3]. The technique of cementing implants was gradually improved, which resulted in better and better results. The cement was supposed to act as a binder allowing to adjust the contour of the implant to the bone bed and immobilize it in relation to the bone. The systems of cement-free endoprostheses were developed in parallel [8-9]. The studies proved that in the case of cement-free solutions, the primary stem implantation should be based on fitting the stem shape to the shape of femoral bone marrow cavity and elimination of the stem micromovements. The first condition was achieved by multiplying stem sizes to fit the size of the femoral bone marrow more precisely. The second problem was solved by various modifications of the stem shape [10-12]. In 1974, Mittelmeier constructed an endoprosthesis, the stem of which was covered with the rib-like structure to improve its fixation in the porous bone structure. The ceramic acetabulum was screwed in and it cooperated with the ceramic modular head. It was one of the first uncemented endoprostheses introduced in clinical practice. Despite the improved solutions, there are still patients using this model of endoprosthesis [3,10-12].

Over the years, it has been demonstrated that the initial tight fit of the stem of the endoprosthesis to the shape of the marrow cavity which provides primary stabilization is sufficient only for a certain period of time [9,11-12]. Under the influence of the transferred loads, the stem micromovements appear over time, leading to the destruction of the bone bed and the consequent loosening of the implant. This led to the development of the concept of secondary stabilization consisting in the implant-bone osteointegration. In order to achieve this objective, the implants were covered with porous coatings with osteoconductive properties, constituting a scaffold for osteogenic cells from the surrounding bone tissue [10-12].

Materiały i metody

Materiał użyty do badań stanowił trzpień endoprotezy Mittelmeiera pozyskany w trakcie operacji rewizyjnej przeprowadzonej 05.07.2017 r. u 67-letniego pacjenta, który został przyjęty do Oddziału Chirurgii Urazowo-Ortopedycznej Szpitala Czerniakowskiego Sp. z o.o. z rozpoznaniem aseptycznego obluzowania trzpienia endoprotezy stawu biodrowego lewego (RYS. 1).

Materials and Methods

The material used in the research was a stem of Mittelmeier's endoprosthesis obtained during the revision operation carried out on 05.07.2017 in a 67-year-old patient who was admitted to the Trauma and Orthopaedic Surgery Department of the Czerniakowski Hospital with the diagnosis of aseptic loosening of the stem of the left hip joint endoprosthesis (FIG. 1).

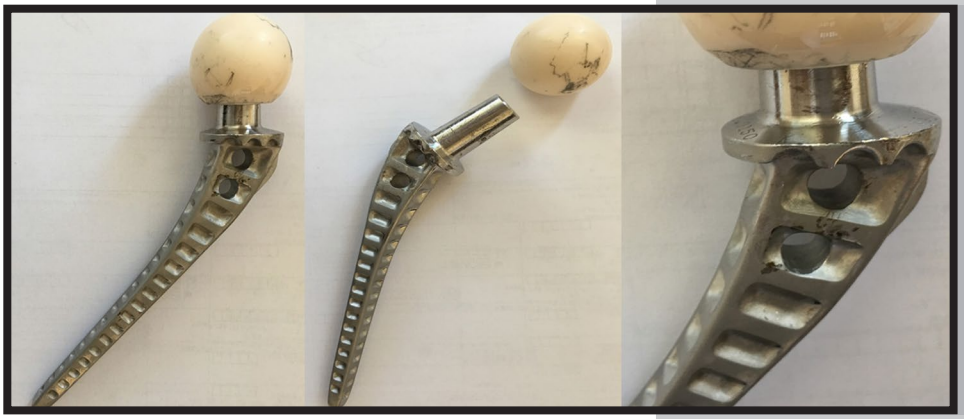

RYS. 1. Deimplantowana endoproteza po 16 latach od wszczepienia [materiał własny].
FIG. 1. Deimplanted endoprosthesis after 16 years of implantation [own material].

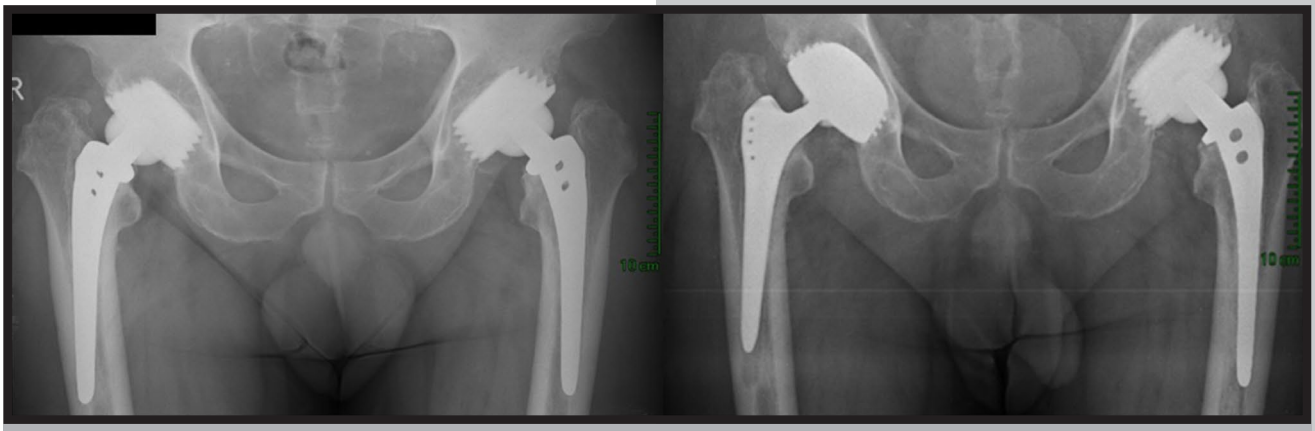

RYS. 2. a) Zdjęcie radiologiczne wykonane w 2010 roku po alloplastyce obu stawów biodrowych, b) Stan po rewizji prawego stawu biodrowego.
FIG. 2. a) Radiological image taken in 2010 following the replacement of both hip joints, b) Condition after a right hip joint re-surgery.

Pacjent ten miał wykonaną obustronną endoprotezoplastykę stawów biodrowych z użyciem bezcementowych endoprotez Mittelmeiera z powodu zmian zwyrodnieniowych. Endoprotezoplastykę prawego stawu biodrowego wykonano w październiku 1999 r. natomiast lewego stawu biodrowego w marcu 2001 r. Z powodu aseptycznego obluzowania w 2010 roku przeprowadzono operacje rewizyjne obu stawów biodrowych (RYS. 2a – obraz przed operacjami rewizyjnymi). W dniu 15.04.2010 r. przeprowadzono rewizję lewego stawu biodrowego – wszczepiono ponownie ten sam trzpień, osadzając go na cemencie chirurgicznym. W dniu 21.10.2010 r. została przeprowadzona realloplastyka prawego stawu biodrowego z zastosowaniem endoprotezy Alloclasic (RYS. 2b – obraz po operacjach rewizyjnych). Na początku 2017 roku pacjent zgłosił się do Szpitala Czerniakowskiego z powodu dolegliwości bólowych biodra lewego z promieniowaniem do uda, nasilających się podczas chodzenia. Obraz kliniczny oraz przeprowadzona diagnostyka laboratoryjna i obrazowa (rtg, scyntygrafia) wykazały obustronne, aseptyczne obluzowanie trzpieni endoprotez stawów biodrowych (RYS. 2b). Chorego zakwalifikowano do ponownej operacji rewizyjnej lewego stawu biodrowego [opracowanie własne].

The patient had double-sided hip joint endoprostheses performed with the Mittelmeier's cementless endoprostheses due to degenerative changes. The right hip endoprosthesis was performed in October 1999 and the left hip in March 2001. Due to aseptic loosening, in 2010 both hip joints underwent re-surgery (FIG. 2a - image before surgery). On 15.04.2010, the left hip joint was extracted and the same stem was reimplanted and placed on surgical cement. On 21.10.2010, right hip realloplasty was performed using the Alloclasic endoprosthesis (FIG. 2b - postoperative image). At the beginning of 2017, the patient was admitted to the Czerniakowski Hospital because of pain in the left hip with radiation to the thigh, which intensified during walking. Clinical picture and laboratory and imaging diagnostics (x-ray, bone scan) showed bilateral aseptic loosening of hip joint endoprostheses (FIG. 2b). The patient was qualified for the second revision of the left hip joint [our study].

W dniu 05.07.2017 r. wykonano endoprotezoplastykę rewizyjną stawu biodrowego lewego – usunięto obluzowany trzpień Mittelmeiera oraz ceramiczną głowę modularną. Nie stwierdzono cech infekcji około protezowej. Nie zaobserwowano cech obluzowania ceramicznej panewki ani uszkodzenia jej powierzchni współpracującej z głową modularną. Usunięto cement chirurgiczny z jamy szpikowej. Po udrożnieniu i rozwierceniu jamy szpikowej osadzono na cemencie chirurgicznym trzpień Taperloc cementowany (RYS. 3) [opracowanie własne].

W celu potwierdzenia przyczyn obluzowania implantu, badaniu poddano trzpień implantu po 16 latach użytkowania. Strukturę analizowanego trzpienia przedstawiają mikrostruktury uzyskane na mikroskopie optycznym Opta-Tech na RYS. 4. W celu ujawnienia mikrostruktury wykonano zgłady metalograficzne, które poddano trawieniu w odczynniku HCl z HNO_3. Zdjęcia mikrostrukturalne metalowego trzpienia (RYS. 5) otrzymano za pomocą mikroskopu skaningowego mikroskopu elektronowego Jeol JSM6610LV. Mikrostruktury SEM obrazujące liczne wżery, pęknięcia oraz ubytki powstałe na skutek zużycia oraz korozji przedstawiono na RYS. 6.

RYS. 3. Stan po reimplantacji trzpienia endoprotezy z dodatkową stabilizacją linkami stalowymi.
FIG. 3. The status after re-implantation of the endoprosthesis stem with additional stabilisation by means of steel cables.

On 05.07.2017, the left hip joint revision endoprosthesis was performed - the loose Mittelmeier stem and the ceramic modular head were removed. No features of the infection were found. No signs of loosening of the ceramic stem or damage to its surface cooperating with the modular head were observed. Surgical cement was removed from the marrow cavity. After unblocking and reaming of the marrow cavity, Taperloc cemented stem (FIG. 3) was placed on the surgical cement [own study].

In order to recognize the causes of implant loosening, the stem was tested after 16 years of use. Microstructures of the analyzed stem surface observed with the optical microscope Opta-Tech are presented in FIG. 4. To reveal the microstructure, metallographic examinations were performed and the sample digested in HCl reagent from HNO_3. Microstructural images of a metal stem (FIG. 5) were obtained with the use of scanning electron microscope Jeol JSM6610LV. SEM microstructures showing numerous pitting, cracks and losses caused by wear and corrosion are presented in FIG. 6.

RYS. 4. Mikrostruktura trzpienia implantu biodrowego.
FIG. 4. The microstructure of the hip implant stem.

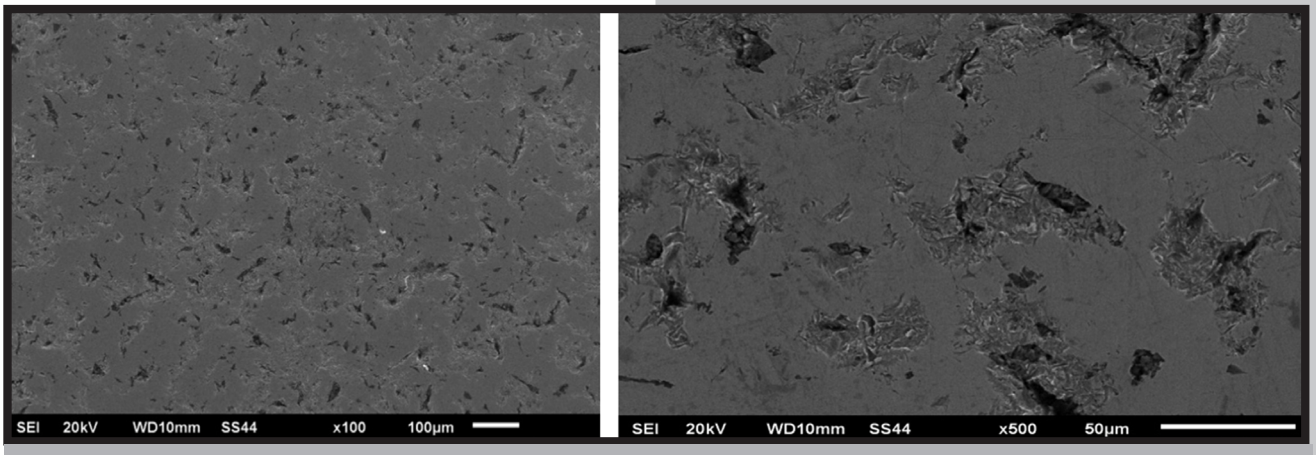

RYS. 5. Wygląd powierzchni trzpienia stawu biodrowego.
FIG. 5. The surface of the hip joint stem.

W kolejnym etapie poddano analizie skład chemiczny trzpienia (TABELA 1) oraz porównano go zgodnie z normą ISO 5832-4 (TABELA 2) [13]. Następnie analizowano skład chemiczny w wybranych miejscach wad i nieciągłości ujawnionych na powierzchni trzpienia z wykorzystaniem skaningowego mikroskopu elektronowego SEM Jeol JSM6610LV zaopatrzonego w przystawkę Oxford EDS. Składy chemiczne oraz mikrostruktury z poszczególnych analiz przedstawiono w TABELACH 3-5.

Na podstawie danych medycznych z Oddziału Chirurgii Urazowo-Ortopedycznej Szpitala Czerniakowskiego Sp. z o.o. w Warszawie wykonano analizę statystyczną przeprowadzonych alloplastyk stawu biodrowego w tym pierwotnych i rewizyjnych oraz występujących powikłań, ze szczególnym uwzględnieniem obluzowań elementów endoprotez, które wymagały operacji rewizyjnych.

In the next stage, the chemical composition of the stem (TABLE 1) was analyzed and compared according to the ISO 5832-4 norms (TABLE 2) [13]. Next, the chemical composition was analyzed in selected areas of defects and discontinuities revealed on the stem surface, using a scanning electron microscope SEM Jeol JSM6610LV equipped with Oxford EDS attachment. Chemical compositions and microstructures from particular analyses are presented in TABLES 3-5.

On the basis of medical data from the Trauma and Orthopaedic Surgery Department of the Czerniakowski Hospital in Warsaw, a statistical analysis of hip joint alloplasty was performed, including primary and revisional surgeries and complications, with particular emphasis on loosening the elements of endoprosthesis.

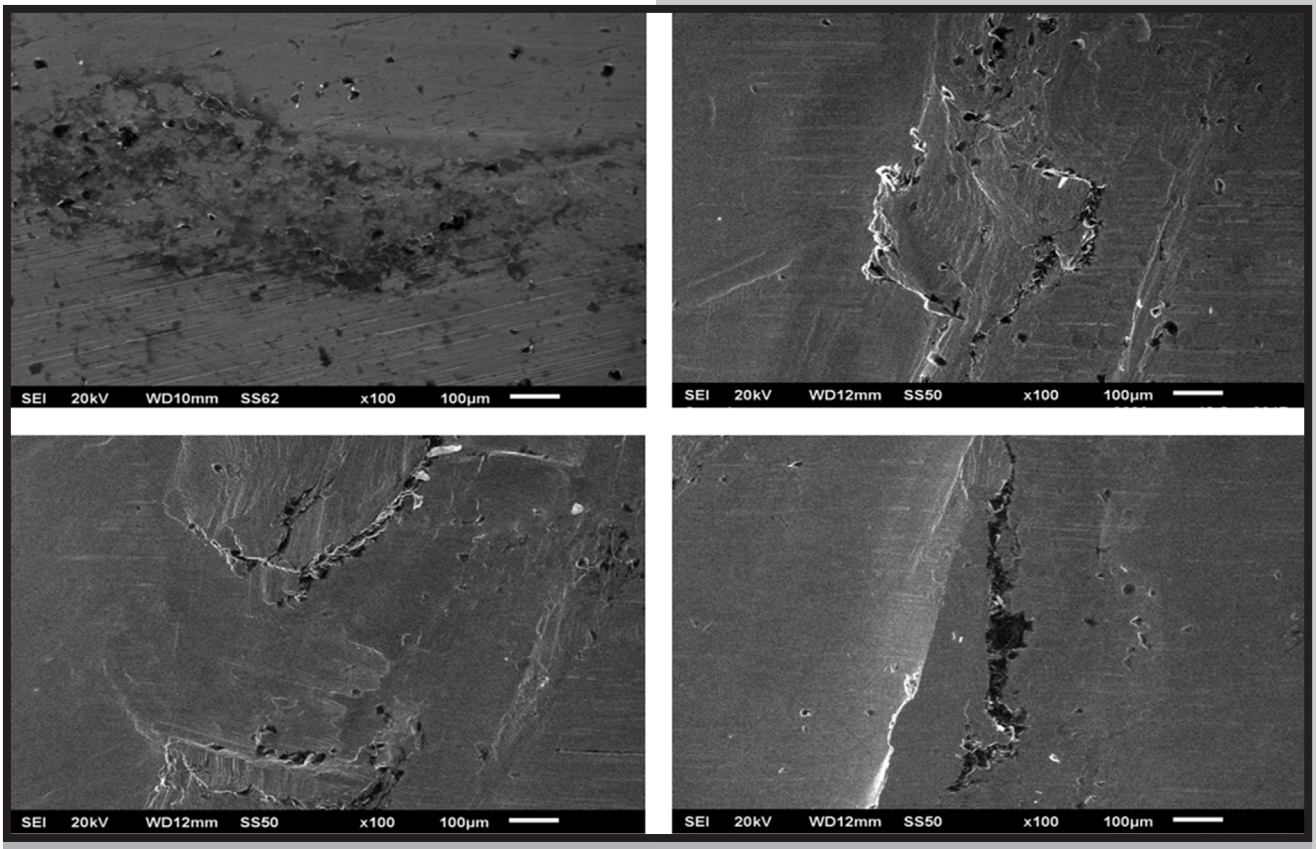

RYS. 6. Powierzchnia trzpienia z licznymi nieciągłościami.
FIG. 6. Stem surface with detected discontinuities.

TABELA 1. Skład chemiczny badanego materiału.
TABLE 1. Chemical composition of the test material.

Pierwiastek Element	Si	Cr	Mn	Fe	Mo	Co
Ilość [% wag.] Content [wt%]	0.78	28.73	1.00	0.50	7.0	reszta balance

TABELA 2. Skład chemiczny stopu według norm ISO 5832-4 (% wag.) [13].
TABLE 2. Chemical composition of the alloy according to ISO standards (wt%) [13].

Stop Vitallium Vitallium alloy	C	Mn	Si	Cr	Ni	Fe	Mo	Co
Skład wg ISO 5832-4 Composition according to ISO 5832-4	max. 0.35	max. 1.0	max 1.0	26.5-30.0	max 2.5	max. 1.0	4.0-7.0	reszta balance

TABELA 3. Skład chemiczny w wybranych miejscach defektu badanego materiału.
TABLE 3. Chemical composition in selected places of the defect of the tested material.

Pierwiastek Element	Si	Cr	Mn	Fe	Mo	Co
Ilość [% wag.] Content [wt%]	0.72	28.89	0.79	0.60	7.06	reszta balance

TABELA 4. Skład chemiczny w wybranych miejscach defektu badanego materiału.
TABLE 4. Chemical composition in selected places of the defect of the tested material.

Pierwiastek Element	0	Na	Mg	Al	Si	P	K	Ca	Cr	Fe	Mo	Co
Ilość [% wag.] Content [wt%]	24.1	0.46	0.36	0.13	0.34	3.96	0.08	2.48	19.14	1.51	3.11	reszta bal.

TABELA 5. Skład chemiczny w wybranych miejscach defektu badanego materiału.
TABLE 5. Chemical composition in selected places of the defect of the tested material.

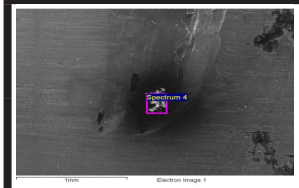

Pierwiastek Element	0	Na	Al	Si	S	Cl	Ca	Cr	Fe	Co
Ilość [% wag.] Content [wt%]	5.71	0.20	0.15	0.24	0.43	0.12	0.53	3.83	1.85	reszta bal.

Wyniki i dyskusja

Mikrostruktura trzpienia implantu przedstawiono na RYS. 4. Badania wykonane na mikroskopie skaningowym prezentuje RYS. 5. Na metalowym trzpieniu ujawniono liczne wżery, pęknięcia oraz ubytki powstałe na skutek zużycia oraz korozji RYS. 6.

Analiza badań materiałoznawczych metalowej endoprotezy wykazała, iż trzpień implantu wykonany jest ze stopu Co-Cr-Mo i posiada strukturę niejednorodnego austenitu, który charakteryzuje się segregacją chemiczną. Badania wykazały, że analizowany materiał charakteryzował się mikrostrukturą dendrytyczną, typową dla stopów odlewniczych. Mikrostruktura badanego stopu była chemiczne niejednorodna. Osnowę stopu kobaltowo-chromowego w stanie lanym stanowił roztwór stały składników stopowych w fazie β-Co. W obrębie krystalitów występowały mikrosegregacje dendrytyczne, w przestrzeniach międzydendrytycznych i wzdłuż granic krystalitów były rozmieszczone wydzielania pierwotne o charakterze ciągłym. Obszary międzydendrytyczne stanowiła eutektyka składająca się z węglików typu $M_{23}C_6$ oraz austenitu kobaltowego β-Co. Stop ten charakteryzował się największą segregacją austenitu (głównie chromu) w obszarze ujawnionych dendrytów. Obecność w stopie chromu ma za zadanie zwiększyć odporność na korozję oraz spowodować samo pasywację stopu. Molibden natomiast wpływa na wzrost odporności na korozję lokalną [16-18].

Wyniki analiz składu chemicznego w miejscach nieciągłości materiału z którego wykonano trzpień dowodzą, że liczne ubytki powstały wskutek dużego zużycia korozyjno-erozyjnego, wpływając bezpośrednio na aseptyczne obluzowanie implantu.

Results and Discussions

The microstructure of the implant stem is shown in FIG. 4. The research performed on the scanning microscope is illustrated in FIG. 5. The metal stem revealed numerous pitting, cracks and losses caused by wear and corrosion of FIG. 6.

The implant stem made of Co-Cr-Mo alloy had a heterogeneous austenitic structure which was characterized by chemical segregation. The examinations showed that the analysed material was of dendritic microstructure, typical of cast alloys. The microstructure of the alloy was heterogeneous. The matrix of the cobalt-chromium alloy in the liquid state represented a solid solution of alloying components in the β-Co phase. There were dendritic microsegregations between crystallites. Furthermore, in the interdendritic spaces and along the boundaries of the crystallites, continuous primary excretions were also found. The interdendritic areas were represented by the eutectic of carbides of $M_{23}C_6$ type and cobalt austenite β-Co. This alloy was characterized by the highest austenite segregation (mainly chromium) in the area of the dendrites. The presence of chromium in the alloy is intended to improve corrosion resistance and cause the alloy to passivate. Molybdenum, on the other hand, increases resistance to local corrosion [16-18].

The results of chemical analysis performed on the stem material discontinuity prove that numerous cavities were caused by high corrosion and erosion wear, directly resulting in the aseptic stem loosening.

TABELA 6. Rodzaje wykonanych alloplastyk stawu biodrowego.
TABLE 6. Types of hip joint alloplasty.

Rodzaj alloplastyki / Type of joint replacement	Liczba / Number	%
Alloplastyki całkowite cementowane / Cemented total hip joint replacements	2	0.3
Alloplastyki całkowite bezcementowe / Cementless total hip joint replacements	460	66
Alloplastyki bipolarne / Bipolar arthroplasty	207	30
Alloplastyki rewizyjne / Revision hip joint replacements	26	3.7
Łącznie / Total	**699**	**100%**

TABELA 7. Wykonane alloplastyki u kobiet i mężczyzn z podziałem na sposób mocowania.
TABLE 7. Alloplastics among women and men with the division of the method of fixing.

Rodzaj alloplastyki / Type of joint replacement	Kobiety / Women		Mężczyźni / Men	
	Number Liczba	%	Number Liczba	%
Całkowita cementowana / Cemented total replacement	2	0.5	0	0
Całkowita bezcementowa / Cementless total replacement	255	59.4	204	75.5
Hybryda / Hybrid replacement	2	0.5	1	0.4
Bipolarna cementowana / Bipolar cemented	3	0.7	0	0
Bipolarna bezcementowana / Bipolar cementless	151	35.2	55	20.4
Rewizyjna cementowana / Cemented revision replacement	6	1.4	2	0.7
Rewizyjna bezcementowa / Cementless revision replacement	10	2.3	8	3.0
Łącznie / Total	**429**	**100%**	**270**	**100%**

TABELA 8. Wskazania do operacji rewizyjnych.
TABLE 8. Indications for re-surgeries.

Wskazania / Indications	Liczba / Number	%
Obluzowanie aseptyczne implantu / Asceptic implant loosening	16	64.3
Obluzowanie septyczne implantu / Septic implant loosening	10	35.7
Łącznie / Total	**26**	**100%**

Na podstawie danych medycznych z przeprowadzonych operacji alloplastyk: całkowitych, bipolarnych i rewizyjnych przeprowadzano analizę statystyczną oraz porównawczą w zależności od płci leczonych pacjentów. Materiał badawczy obejmował okres od 2014 do 2018 roku i pochodzi z Oddziału Chirurgii Urazowo-Ortopedycznej Szpitala Czerniakowskiego Sp. z o.o. w Warszawie.

Obejmuje on 699 alloplastyk stawów biodrowych (TABELA 6), w tym:
1. Alloplastyk całkowitych cementowanych: 2 (0,3%)
2. Alloplastyk całkowitych bezcementowych: 460 (66%)
3. Alloplastyk bipolarnych: 207 (30%)
4. Alloplastyk rewizyjnych: 26 (3,7%)

Biorąc pod uwagę płeć operowanych pacjentów, wykonano 429 alloplastyk stawu biodrowego u kobiet oraz 270 u mężczyzn. TABELA 7 przedstawia liczbę oraz udział procentowy poszczególnych rodzajów alloplastyk z podziałem na płeć leczonych chorych.

W tym czasie wykonano 26 operacji rewizyjnych (TABELA 8). W 64,3% ich powodem było obluzowanie aseptyczne implantu, natomiast w 35,7% spowodowane one były obluzowaniem septycznym. Wśród reoperowanych pacjentów stwierdzono 5 przypadków obluzowań panewki i 3 obluzowania trzpienia endoprotezy, jednak dwa z nich wystąpiły po 12 latach od wszczepienia implantu. W 8 przypadkach doszło do zwichnięcia endoprotezy, do czego przyczynić się mogło niestosowanie się pacjentów do zaleceń lekarskich. Stwierdzano również przypadki złamań około protezowych trzonu kości udowej, powodujące destabilizację trzpienia endoprotezy [14-15].

On the basis of medical data from alloplastic surgeries: total, bipolar and revision surgeries, a statistical and comparative analysis was performed depending on the sex of the patients. The research material covered the period from 2014 to 2018 from the Department of Trauma and Orthopaedic Surgery of the Czerniakowski Hospital in Warsaw.

The data includes 699 hip joint alloplasty (TABLE 6), of which:
1. Cemented total hip joint replacements: 2 cases (0.3%)
2. Cementless total hip joint replacements: 460 cases (66%)
3. Bipolar arthroplasty: 207 cases (30%)
4. Revision hip joint replacements: 26 (3.7%)

Taking into account the sex of the patients, 429 hip joint replacements were performed in women and 270 in men. TABLE 7 presents the number and percentage of particular types of hip joint replacements regarding the sex of patients.

During this time, 26 re-surgeries were carried out (TABLE 8). The aseptic loosening of the implant was the cause of 64.3% of all the surgeries, while the septic loosening of the implant was the cause of 35.7%. Among the re-operated on patients, 5 cases of acetabulum loosening and 3 cases of endoprosthesis stem loosening were found, however, two of them occurred 12 years after the implantation. In 8 cases the endoprosthesis dislocation occurred, which may have been caused by patients' failure to follow the medical recommendations. There were also cases of approximate femoral stem fractures causing destabilization of the stem of the endoprosthesis [14-15].

Podsumowanie

Przeprowadzone badania wykazały, że nie tylko implant osadzony w kości oddziałuje na okoliczne tkanki. Zachodzą również zmiany w obrębie wszczepionego implantu. Dlatego należy nadal poszukiwać optymalnych pokryć ortopedycznych z uwzględnieniem wzajemnych interakcji zachodzących między żywymi tkankami i implantem. Przeprowadzona analiza składu chemicznego ujawniła, iż udział procentowo-wagowy poszczególnych pierwiastków jest zgodny z normą ISO 5832-4. Analiza badań materiałoznawczych metalowej endoprotezy wykazała, iż trzpień implantu wykonany jest ze stopu Co-Cr-Mo i posiada strukturę niejednorodnego austenitu. Stop ten charakteryzował się największą segregacją austenitu (głównie chromu) w obszarze ujawnionych dendrytów. Analiza materiałoznawcza ujawniła na metalowym trzpieniu liczne wżery, pęknięcia oraz ubytki powstałe na skutek zużycia korozyjno-erozyjnego. Przyczyną obluzowania aseptycznego implantu była osteoliza związana z nagromadzeniem w przestrzeni pomiędzy implantem a kością elementów zużycia korozyjnego i erozyjnego. W analizowanym materiale danych klinicznych wykazano, iż wiodącym wskazaniem do wykonania alloplastyki bipolarnej jest złamanie szyjki kości udowej, występujące najczęściej u kobiet. Alloplastykę całkowitą wykonuje się w przypadku zmian zwyrodnieniowych lub jałowej martwicy głowy kości udowej. Jak wynika z analizowanych danych, liczba wykonywanych alloplastyk stawu biodrowego stale rośnie i zalicza się je obecnie do najczęstszych operacyjnych procedur ortopedycznych. Nadal nierozwiązane są problemy występujących powikłań septycznych i aseptycznych, co rodzi konieczność prowadzenia badań m.in. nad udoskonalaniem właściwości użytkowych implantów w celu redukcji obserwowanych powikłań.

Podziękowania

Szczególne podziękowania kieruję do Szpitala Czerniakowskiego Sp. z o.o. za udostępnienie implantu do badań oraz danych klinicznych dotyczących operacji endoprotez stawu biodrowego.

Conclusions

Research has shown that it is not only the bone implant that affects the surrounding tissue. There are also changes in the area of the implanted prosthesis. Therefore, optimal orthopaedic coatings should still be researched on, taking into account the interactions between living tissues and the implant. The chemical composition analysis revealed that the percentage by weight of individual elements complies with the ISO 5832-4 norm. The materials analysis of the metal endoprosthesis showed that the implant stem is made of the Co-Cr-Mo alloy and it has a structure of heterogeneous austenite. This alloy is characterized by the highest segregation of austenite (mainly chromium) in the area of dendrites. The microstructure analysis revealed numerous pits, fractures and losses caused by corrosion and erosion wear on the metal stem. The cause of aseptic implant loosening was osteolysis in the space between the implant and the bone associated with the accumulation of elements of corrosion and erosion wear. The clinical data showed that the main indication for bipolar alloplasty is femoral neck fracture, most common in women. Total alloplasty is performed for degenerative changes or sterile femoral head necrosis. The analyzed data clearly proves that the number of hip endoprostheses implantations is constantly growing and it is currently one of the most common orthopaedic surgical procedures. The problems of existing septic and aseptic complications are still unsolved, which raises the need for research, among others on improving the functional properties of implants to reduce the observed complications.

Acknowledgements

Special thanks go to the Hospital Czerniakowski Sp. z o. o. for providing the implant for research and clinical data on hip endoprostheses surgery.

References

[1] Lawrence D.: Alloplasty of the hip joint. Edra Urban&Partner, Wroclaw, 2017.
[2] Pozowski A.: Alloplasty of the hip joint. Publishing House, Medical Publishing House, Warsaw 2018.
[3] Kmieciak M., Panasiuk M.: History and development of hip prosthetic surgery. Part I. Kwart. Orthop., 3 (1993).
[4] Smith-Petersen M.N.: Arthroplasty of the hip. J. Bone Joint Surg., 21 (1939).
[5] Golec E., Nowak S., Golec J., Jurczak P., Abrowski J.: Periprosthetic fractures as complications of total hip joint alloplasty - distant results of treatment and rehabilitation (in Polish). Kwart. Ortop. 3 (2006) 210-216.
[6] Kordasiewicz B., Rylski W., Zakrzewski P., Sawicki G., Orłowski J., Pomianowski S.: Total dislocations of hip joint endoprostheses. Chir. Narz. Orthopaedic Movement. Pol. 5 (2004) 69-325.
[7] Golec E., Nowak S., Golec J., Abrowski J., Jasiak-Tyrkalska B.: Dislocations of hip joint endoprostheses. Chir. Orthopaedic Movement Gallus. Pol. 3 (2006) 71-187.
[8] Jędrzejczak M., Synder M., Marciniak M., Koza B.: Assessment of the quality of life of patients after hip joint alloplasty (in Polish). Kwart. Ortop. 4 (2001) 228-234.
[9] Barn B.: Cement hip joint endoprosthesis ORTOMED. Quarter. Orthopaedic 2 (2001).
[10] Przedborska A., Kopeć J., Smyj K.: Evaluation of early results of cement alloplasty as a method of treatment of advanced hip arthritis (in Polish). Kwart. Ortop. 1 (2006) 44-54.
[11] Williams J.T., Regland P.S., Clarke S.: Constrained for the unstable hip following total hip arthroplasty: a literature review. Int. Orthop. 31(3) (2007) 273-277.
[12] Kopyś J., Pozowski A., Cieszyński J.: Comparison of the process of osteointegration of cementless panes covered with hydroxyapatite or sputtered with titanium. Ortopedia Traumatologia Rehabilitacja 6 (2004), Supplement 1.
[13] https://www.iso.org/obp/ui/#iso:std:iso:5832:-4:en.
[14] Sienkiewicz D., Golec E., Nowak S., Golec J., Szczygieł E., Plewa A.: Evaluation of the results of distant surgical treatment of femoral percutaneous fractures with the use of dynamic hip stabilizer. Review. Medicine 1 (2008) 32-65.
[15] Widawski A., Golec E., Nowak S.: Remote results of X-change revision of hip joint alloplasty. Surgery. Narz. Orthopaedic movement. Pol. 3 (2003) 68-165.
[16] Marciniak J.: Biomaterials, Publishing House of the Silesian University of Technology, Gliwice 2013.
[17] Dudek A.: Forming useful properties of metallic and ceramic biomaterials, Publishing House of Częstochowa University of Technology, Częstochowa 2010.
[18] Dąbrowski J. R.: Co-Cr-Mo alloyed sintered biomaterials, Warsaw University of Technology Publishing House, Warsaw 2004.

SYNTHESIS AND STRUCTURAL CHARACTERIZATION OF NIOBIUM-DOPED HYDROXYAPATITE CERAMICS

Wojciech Korzeniewski*, Agnieszka Witkowska*

Department of Solid State Physics,
Gdansk University of Technology,
Narutowicza 11/12, 80-233 Gdansk, Poland
*e-mail: wojciech.korzeniewski@pg.edu.pl,
agnieszka.witkowska@pg.edu.pl

Abstract

Hydroxyapatite (HAp) ceramic materials are considered as one of the most promising implant materials in bone surgery and in dentistry. They exhibit unique biocompatibility, bioactivity, and osteoconductivity, which are the most desirable biomaterial features. However, HAp itself is brittle, has low strength, high degree of crystallinity and low solubility at physiological pH. Doping synthetic HAp with metal ions plays an important role in improving its structural and physico-chemical properties. HAp doped with niobium ions has not been widely investigated so far. However, the results of studies available in the literature show that the synthesized CaO-P_2O_5-Nb_2O_5 compounds still show good biocompatibility, very low cytotoxicity and, additionally, they stimulate osteoblast proliferation. Therefore, this study is dedicated to the niobium-doped HAp ceramics obtained by two methods: mechano-chemical synthesis and sol-gel method. Bioceramics chemical composition, morphology, and structure were characterized by means of scanning electron microscopy imaging, BET method, X-ray diffraction, Fourier transform infrared spectroscopy and X-ray photoelectron spectroscopy. The results indicate that nanoceramics of non-stoichiometric HAp with a clear Ca deficiency on the nanograin surface were obtained. Moreover, it has been observed that the presence of Nb dopants and the synthesis method directly affect unit cell parameters, crystallinity degree, crystallites size, porosity and distribution of niobium in the grain structure. Mechano-chemical synthesis has allowed effective niobium incorporation into the HAp structure, leading to the quite homogeneous Nb distribution in the grain volume. Whereas, Nb-doping by sol-gel method has led to dopants location mainly on the grain surface.

Keywords: *structure, nanoceramics, mechano-chemical synthesis, sol-gel method, hydroxyapatite, niobium*

[Engineering of Biomaterials 150 (2019) 10-15]

Article presented at conference: IMPLANTS 2019, 28-29 June, Gdansk, Poland.

Introduction

Apatites are the most important and most abundant components of hard human tissues. For that reason, these materials have been objects of intensive research for the last decades. In this group hydroxyapatite (HAp) ceramics is the most promising material because its chemical composition is similar to that of a natural bone. Furthermore, it exhibits biocompatibility, bioactivity and osteoconductivity, which are one of the most desirable biomaterial characteristics [1,2]. For these reasons, HAp is widely used in medical applications, for example as bone graft substitutes, in drug delivery systems and hypodermic devices. In addition, hydroxyapatite thin layers on metal implants significantly improve biological properties of these systems [3].

Depending on the HAp application, different properties of this material are required. These properties are strongly related to the structure, morphology and chemical composition of the obtained material. Currently, many methods of hydroxyapatite synthesis are used to precisely define the properties of the obtained ceramics. However, a versatile method of synthesis is of interest as it gives the possibility to in-build other ions, organic elements or drugs into the HAp structure in an easy manner and at low temperature. The methods of HAp synthesis can be divided into: i) dry methods – in which the material is a result of a solid state reaction of precursors and ii) wet methods – in which reaction occurs in mixtures of solutions of precursors [4]. Among the wet methods the precipitation should be mentioned as the most frequently used and the sol-gel technique. The latter one is becoming more and more popular because it allows nanocrystalline materials to be created and chemically modified (by, for example, doping with ions) in a relatively easy way [5,6].

The main disadvantages of hydroxyapatite are brittleness and low strength. Other drawbacks include design limitations, a high degree of crystallinity which results in low solubility in physiological pH and non-biodegradability. Thus, a substantial effort has been devoted to improve synthetic HAp structural and physico-chemical properties. One of the strategies, still used, is doping HAp with ions [7]. Various substitutions are used, namely cationic (e.g. using magnesium, strontium, zinc), anionic (e.g. using carbonates, fluorides, silicates) and multi-ionic. For instance, strontium doped HAp exhibits greater hardness and compressive strength. On the other hand, magnesium-doped HAp shows a slight deterioration of these properties but the improved fracture toughness [8]. HAp doped with niobium ions has not been extensively investigated up to now. The results found in the literature [9-11] show that synthesized CaO-P_2O_5-Nb_2O_5 compounds exhibit good biocompatibility, very low cytotoxicity when compared to calcium-phosphate doped with other metals and they can enhance human osteoblast function. Moreover, they have promising mechanical parameters. For these reasons, Nb-doped HAp has the potential to be used as a biomaterial in bone tissue repair [9] and as a buffering layer between metal implants and natural tissue.

In this paper, we compare structural and morphological properties of pure hydroxyapatite and niobium-doped hydroxyapatite prepared via a dry method – the mechano-chemical synthesis and a wet method – the sol-gel technique.

Materials and Methods

Synthesis

In this paper, hydroxyapatite powders were synthesized by two methods: the mechano-chemical synthesis and the sol-gel method. In this way, undoped and Nb-doped powders were obtained. The amount of dopant was set at 10 mol% of phosphorus.

In the mechano-chemical synthesis, stoichiometric amounts (i.e. molar ratios Ca/P and Ca/(P+Nb) of 1.67) of calcium hydroxide ($Ca(OH)_2$), diammonium hydrogen phosphate ($(NH_4)_2HPO_4$) and niobium pentoxide (Nb_2O_5) were used as precursors. First, the powders were quickly mixed and ground in an agate mortar. Next, they were milled in the planetary ball mill using rotation speed of 400 rpm for 16 h (including an hour of break after each hour of milling). Lastly, the samples were ground in a mortar to obtain fine powders. The studied samples are referred to as: MS-HAp (undoped material) and MS-Nb-HAp (niobium-doped material).

In the sol-gel method ethanol solutions of calcium nitrate tetrahydrate ($Ca(NO_3)_2 \cdot 4H_2O$), phosphorus pentoxide (P_2O_5) and niobium (V) chloride ($NbCl_5$) were used as precursors. The amounts of substrates were chosen to obtain a stoichiometric material (i.e. molar ratios Ca/P and Ca/(P+Nb) of 1.67). To obtain the solutions, a calcium-containing precursor was dissolved in a beaker containing 50 ml of ethanol and phosphorus- and niobium-containing precursors (or only phosphorus in the case of an undoped sample) were dissolved together in a separate beaker containing 50 ml of ethanol. The solutions were mixed and stirred at room temperature. Gelation of the mixtures occurred in a water bath at 60°C. Gel aging and drying at 80°C lasted for 24 h. The dried gels were sintered at 700°C with heating and cooling speed rates of 10°C/min and then ground in an agate mortar. These powders are referred to as: SG-HAp (undoped material) and SG-Nb-HAp (niobium-doped material).

Characterization

The morphology and composition of powders were analyzed under FEI Quanta FEG 250 scanning electron microscope (SEM) with energy dispersive spectroscopy (EDX) system. EDX results were averaged from three (or more) 1200 μm x 1000 μm area analyses, the acquisition time for each analysis was set at 50 s. Then, a molar ratio of Ca/(P+Nb) was calculated (for stoichiometric hydroxyapatite this ratio equals 1.667 [1]). For SEM imaging the samples were gold coated by sputtering, to avoid charging.

The surface area was investigated by adsorption of nitrogen at 77 K (Quantachrome Autosorb IQ-Chemisorption & Physisorption Gas Sorption Analyzer) according to the BET method. Prior to the analysis the powders were degassed for 3 h at 150°C.

The X-ray diffraction (XRD) of the powders was performed using Philips X'Pert-MPD X-ray Diffraction System operating with CuKα radiation in the 2θ range of 20-55° and with scan step size of 0.02°. Based on the XRD pattern, the samples phase compositions were determined and the crystallites size, lattice parameters as well as unit cell volumes were estimated.

The investigation of functional groups was done by Fourier transform infrared (FTIR) spectroscopy using PerkinElmer FT-IR/FIR Spectrometer Frontier in attenuated total reflectance (ATR) mode in the range of 550-4000 cm^{-1} with scan step size of 1 cm^{-1} and resolution of 2 cm^{-1}.

The surface composition was analyzed by X-ray photoelectron spectroscopy (XPS) using Omicron XPS operating with Mg anode, achromatic radiation, scan step size of 0.05 eV and pass energy of 50 eV. The effects associated with the charge loading of samples were removed by calibrating to the carbon C1s band (284.5 eV) [12,13]. The elemental composition analysis and decomposition of the obtained bands were carried out using the CasaXPS software [14].

Results and Discussions

The SEM images of obtained powders are shown in FIG. 1 and the results of their detailed analysis and EDX measurements are presented in TABLE 1. As it can be observed, both the undoped powders are composed of sphere-like nanograins approximately 100 nm (MS-HAp) and 50-200 nm (SG-HAp) in diameter. Additionally, in the SG-HAp sample, particles with morphology of whiskers - measuring about 200 nm in length - are also observed. This suggests the possible presence of two different calcium-phosphate phases in the compound, with one of them of the Ca/P molar ratio evidently lower than 1.5. The doped MS-Nb-HAp sample also consists of sphere-like nanograins (diameters of approximately 100-300 nm), but these grains form a rather solid porous structure (with the expanded surface and complex porosity). The SG-Nb-HAp sample has a solid structure that is highly porous and the pore size distribution is narrow, with the mean micropores' size of about 100-250 nm in diameter. These results show that the addition of niobium affects the morphology of hydroxyapatite materials, in general changing it from granular to a more solid one and increasing the sample porosity. However, the details of the morphology are strongly dependent on the synthesis procedure.

Only in the case of the SG-Nb-Hap sample the EDX analysis detected the trace amounts of chlorine - the residual substrate used for nobium doping, no other elements or impurities were registered apart from the elements related to the assumed material composition (P, Ca, Nb and O). Additionally, it was revealed that the relation between the main elements of synthesized powders differs from the target one (Ca/(P+Nb) = 1.667). The results also indicate that doping through the mechano-chemical synthesis is more efficient than through the sol-gel process. The obtained molar ratio of Nb/P was 0.08 and 0.04 for the samples of MS-Nb-HAp and SG-Nb-HAp, respectively.

To check the SEM visible morphology changes induced by doping, the N_2 adsorption isotherms of prepared powders were collected and used to calculate the BET surface area. The results are shown in FIG. 2 and TABLE 2. The undoped powders had a relatively small BET surface area. Doping with niobium increased the BET surface area to 31.02 m^2/g for the Hap sample prepared via the mechano-chemical synthesis (with the value six times higher than for the undoped material) and to 10.35 m^2/g for the sample synthesized using the sol-gel method (the increase by only 15% in respect to the undoped material). These results, like the SEM results, suggest that doping affects the powders morphology, but in the case of the mechano-chemically synthesized powders, it causes a greater surface development than when using the sol-gel method.

The XRD patterns of the powders are shown in FIG. 3. The diffraction peaks are mainly indexed to the hexagonal HAp phase (PDF#74-0566), confirming the synthesis of the non-stoichiometric form of hydroxyapatite (see TABLE 1). The hexagonal unit cell parameters derived from the XRD patterns analysis and unit cell volumes are presented in TABLE 3. Only in the SG-HAp sample additional peaks corresponding to the presence of other calcium-phosphate phase, with a lower Ca/P molar ratio (PDF#70-2065), were detected (peaks marked by X in FIG. 3). This result perfectly correlated with the grains shaped as nanowhiskers observed in the SEM images (see FIG. 1c).

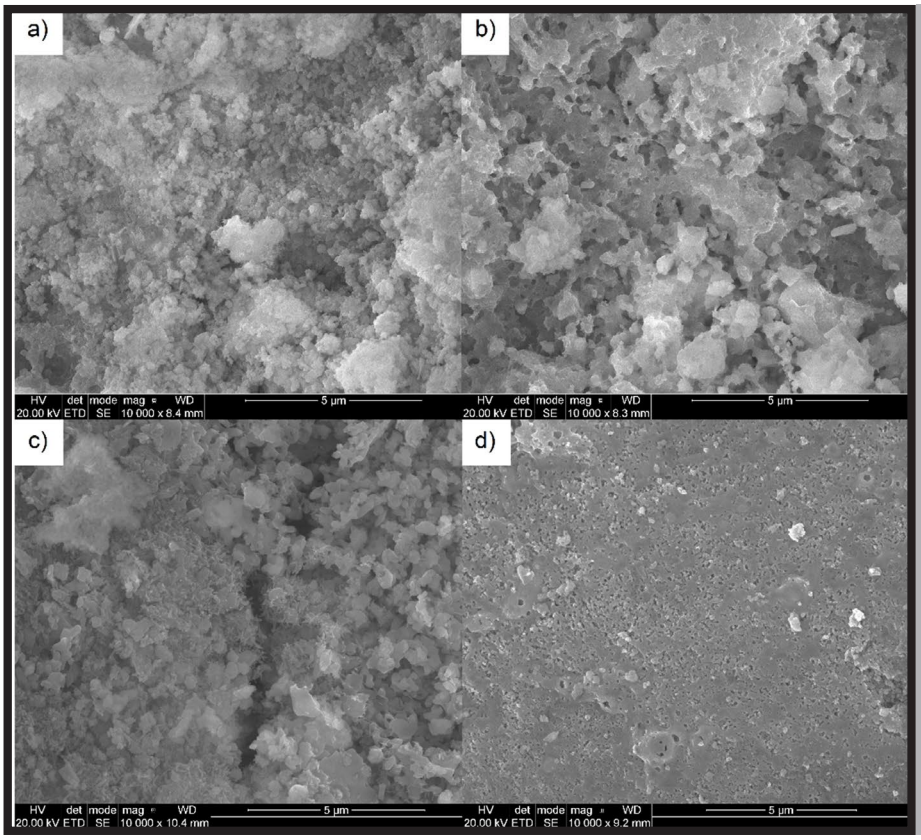

FIG. 1. SEM images of synthesized powders:
a) MS-HAp,
b) MS-Nb-HAp,
c) SG-HAp,
d) SG-Nb-HAp.

TABLE 1. SEM imaging and EDX analysis results.

Sample	Size [nm]	Ca/(P+Nb) molar ratio	Nb/P molar ratio
MS-HAp	**Nanograins** 100	1.53 ± 0.08	-
MS-Nb-HAp	**Nanograins** 100-300	1.77 ± 0.09	0.08
SG-HAp	**Nanograins** 50-200 **Nanowhiskers** 200	1.52 ± 0.08	-
SG-Nb-HAp	**Pores** 100-250	1.68 ± 0.09	0.04

TABLE 2. BET surface areas of synthesized powders.

Sample	BET surface area [m^2/g]
MS-HAp	5.36
MS-Nb-HAp	31.02
SG-HAp	8.97
SG-Nb-HAp	10.35

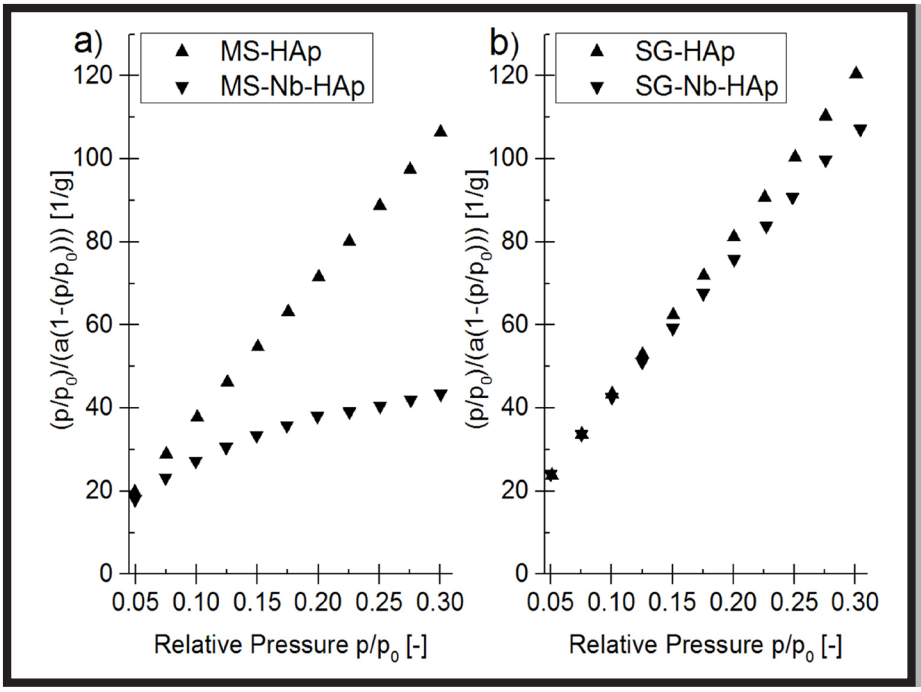

FIG. 2. N_2 adsorption isotherms, used for BET analysis, of powders synthesized through:
a) mechano-chemical synthesis,
b) sol-gel method.

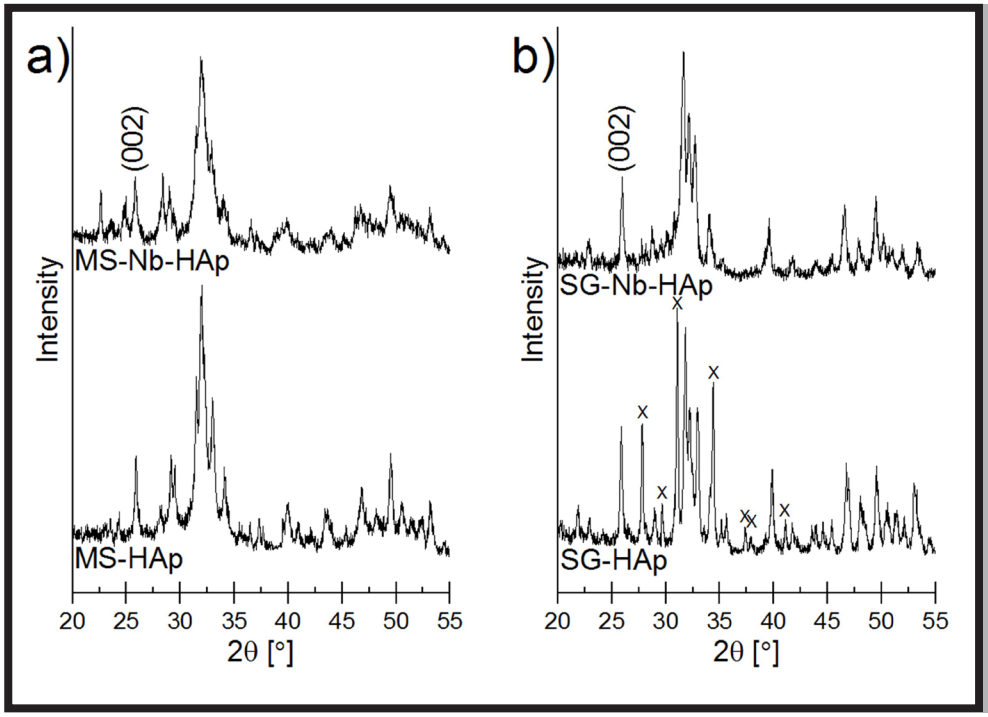

FIG. 3. XRD patterns of powders synthesized through:
a) mechano-chemical synthesis,
b) sol-gel method.
X – the second phase with lower Ca/P molar ratio.

TABLE 3. Crystallite sizes, lattice parameters and unit cell volumes of prepared powders obtained by XRD patterns analysis.

Sample	Crystallite size [nm]	Lattice parameters [Å] (hexagonal)	Unit cell volume [Å^3]
MS-HAp	24.90 ± 0.55	a = b = 9.40(1) c = 6.89(1)	526.85
MS-Nb-HAp	18.80 ± 0.33	a = b = 9.41(1) c = 6.90(1)	528.99
SG-HAp	33.11 ± 0.92	a = b = 9.43(1) c = 6.89(1)	529.34
SG-Nb-HAp	26.12 ± 0.60	a = b = 9.48(1) c = 6.86(1)	533.31

In the XRD measurements, the most visible effects of Nb doping were the crystallinity degree decrease, broadening of diffraction peaks (independently on the sample preparation procedure) and the disappearance of the additional phase observed in the material prepared by sol-gel method. The peaks broadening effect indicates the decrease in the mean crystallite size. The size was determined by the Sherrer formula and the results obtained for all the samples are presented in TABLE 3. The calculations were performed using (002) peak parameters (peak marked in FIG. 3). It should be emphasized that crystallite sizes in the undoped HAp were in the range of 25-35 nm and doping actually reduced this value to 18-27 nm. Nevertheless, the unit cell volume of the samples increased due to doping. Moreover, in the XRD pattern of the Nb-doped samples additional peak at 22.8° appeared (with a higher relative intensity in the MS sample), which can indicate that Nb was effectively incorporated into the hexagonal HAp structure (PDF#72-1484 – hexagonal niobium oxide phase).

The FTIR spectra of obtained powders are shown in FIG. 4. In all the samples, the characteristic peaks of HAp were observed. The intense band appearing at roughly 1020 cm^{-1} and the less intense band at 940 cm^{-1} were assigned to the asymmetric (v_3) and symmetric (v_1) stretching modes in the $(PO_4)^{3-}$ anions, respectively [15]. Moreover, in the FTIR spectra of undoped samples and the MS-Nb-HAp v_3 the vibration mode of $P(OH)_2$ groups located at approximately 1000 cm^{-1} and a very weak and broad absorption band of the $(HPO_4)^{2-}$ groups located at 740 cm^{-1} was also noted [15].

The presence of $(HPO_4)^{2-}$ anions serves as an indirect confirmation of the non-stoichiometricity of the obtained hydroxyapatite materials. The broad bands at around 3220 cm^{-1} and 2850 cm^{-1} are associated with the vibration modes of H-O-H bonds of water adsorbed on the powders and the stretching modes of N-H bonds in the ammonium groups, respectively [15]. Both bands are visible for the mechano-chemically synthesized materials (FIG. 4a). The N-H vibration bands are non-existent in the SG materials (FIG. 4c) because none of the substrates used in their synthesis contained ammonia or its compounds. Moreover, in the spectra of MS materials, the presence of a band located at about 3600 cm^{-1}, attributed to the stretching vibration of the OH^- functional groups inbuilt in the HAp lattice [15], should be underlined. In addition, the carbonate bands located at approximately 1440 cm^{-1} and 860 cm^{-1} are observed in the FTIR spectra [15]. They might come from the atmosphere carbon compounds which combined with the HAp structure during synthesis. This effect is much more pronounced in the case of mechano-chemical synthesis. The detailed analysis revealed that CO_3^{2-} ions introduced into the structure of HAp mainly substituted the PO_4^{3-} ions. This phenomenon may additionally improve the biological activity of HAp, as the carbonated HAp is essential for bonding with natural bone [16].

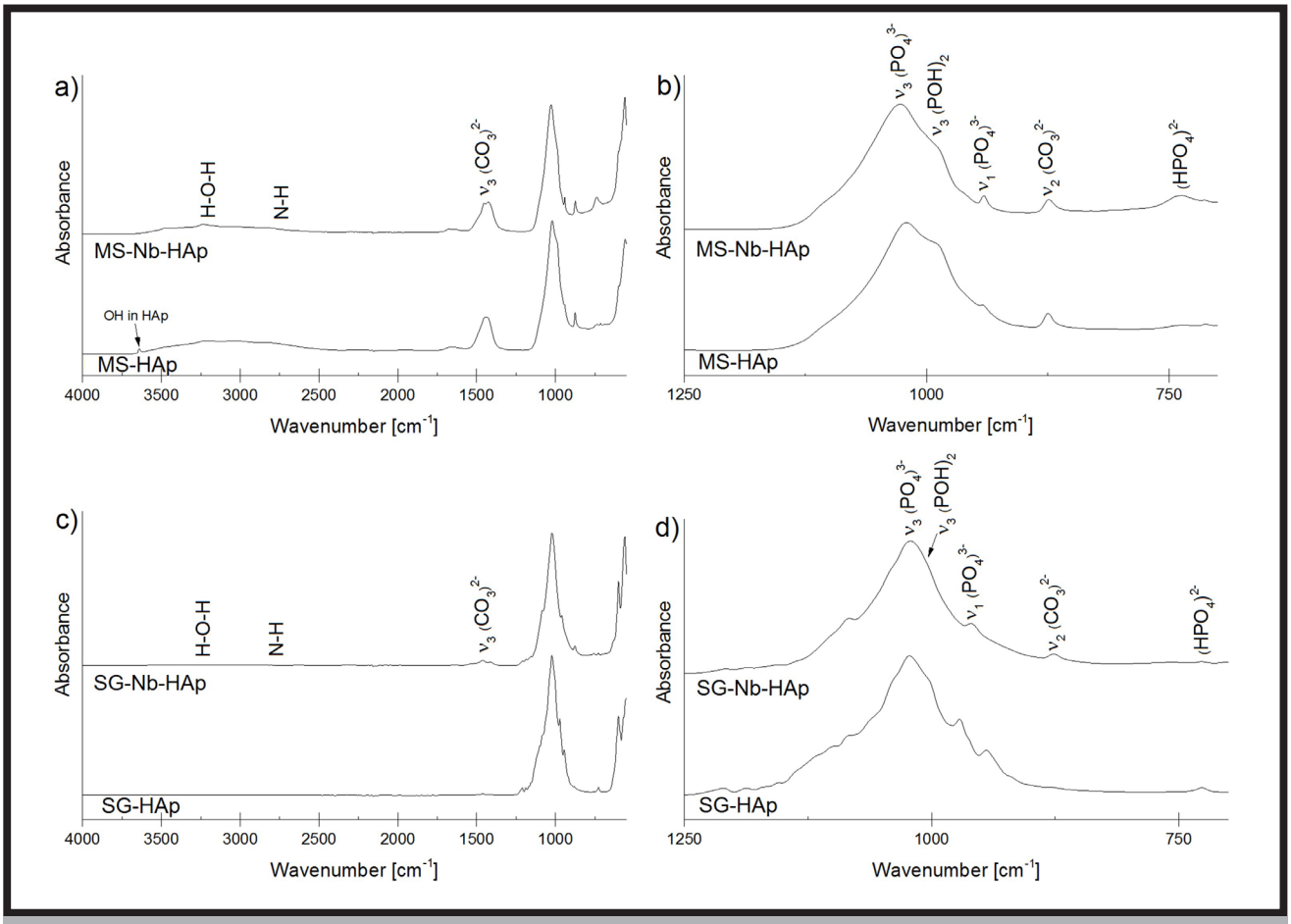

FIG. 4. FTIR spectra of powders synthesized through: a)-b) mechano-chemical synthesis and c)-d) sol-gel method.

TABLE 4. XPS quantitative analysis results.

Sample	Ca/(P+Nb) molar ratio	Nb/P molar ratio	$Nb^{+5}/(Nb^{+5}+Nb^{+4})$ [%]
MS-HAp	1.06 ± 0.1	-	-
MS-Nb-HAp	0.96 ± 0.1	0.02	68(10)
SG-HAp	1.05 ± 0.1	-	-
SG-Nb-HAp	1.29 ± 0.1	0.07	80(5)

Using the XPS spectra, a quantitative analysis was carried out, based on the decomposition of Ca2p, P2p, and Nb3d bands. The results of this analysis presented in TABLE 4 show that the surface of the grains of all the samples exhibits calcium deficiency, independently from the method of synthesis and Nb presence. This Ca deficiency equals 30% in the case of the undoped powders and after Nb-doping it increases to 45% and decreases to 23% for the materials prepared by the MS and the SG method, respectively. At the same time, in the MS-Nb-HAp sample the pronounced decrease in Nb surface concentration is noted, whereas in the SG-Nb-HAp sample this concentration increases with respect to volume value (compare Nb/P data presented in TABLES 1 and 4). The detailed Nb3d line decomposition unveiled the presence of two niobium valency states, Nb^{+5} [17] and Nb^{+4} [18], as shown in FIG. 5.

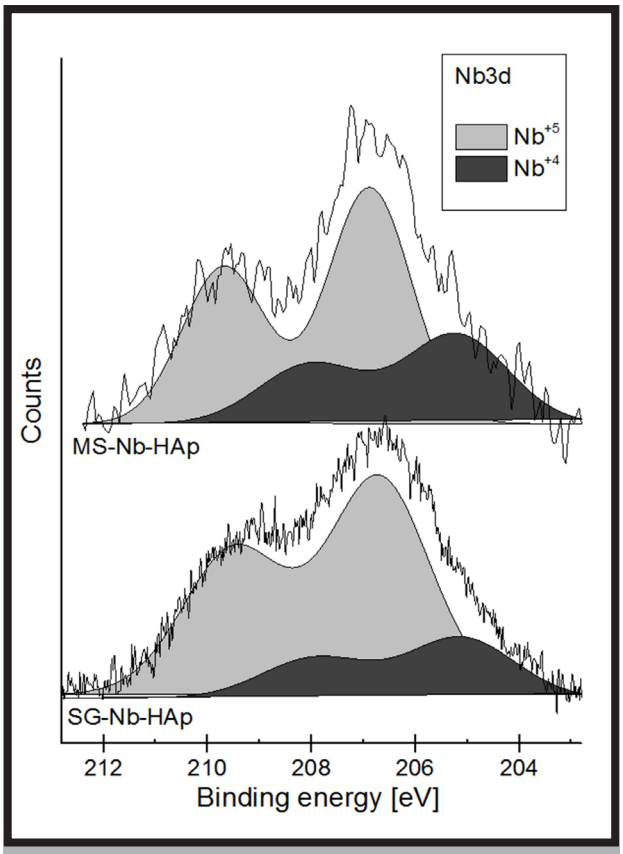

FIG. 5. Nb 3d XPS spectra decomposition performed for Nb-doped nanoceramics.

However, in either sample the Nb^{+5} state dominates and its contribution is almost the same in terms of uncertainty range (about 70% and 80% in the MS-Nb-HAp and the SG-Nb-HAp, respectively, see TABLE 4). These results confirm that the mechano-chemical synthesis allows effective niobium incorporation into the HAp structure (in the nanograins core the Nb/P molar ratio reaches nominal value, i.e. ~10%). Whereas, Nb doping by the sol-gel technique resulted in dopants location on the sample surface rather than in the sample volume. The additional XPS spectra analysis on the O1s band confirms that the dominant calcium-phosphate phase on the sample surface is the phase with the Ca/(P+Nb) molar ratio of approximately 1.0.

Conclusions

In the paper, the results of the structural characterization of the niobium-doped HAp ceramics obtained by either the mechano-chemical synthesis or the sol-gel method, are presented and compared. The results showed that nanoceramics of non-stoichiometric HAp with the surface Ca deficiency were obtained. However, in the sol-gel technique the presence of two crystalline calcium-phosphate phases - one hexagonal HAp phase and another one with Ca/P molar ratio lower than 1.5 - were detected. The Nb-doping process, independently from the synthesis method, caused the changes in the unit cell parameters, manifested in the increase in the volume of the unit cell, the decrease in the crystallinity degree and the average crystallites size and the slight increase in the material active surface area. The detailed analysis demonstrated that niobium (mainly in forms of Nb^{5+} species) was more effectively incorporated into the hydroxyapatite structure by the mechano-chemical method than by the sol-gel approach. This is evidenced by a different distribution of niobium in the grain structure. The mechano-chemical synthesis led to obtaining a quite homogeneous Nb distribution in the volume of the grains, whereas the sol-gel method resulted in the dopants location dominant on their surface. In terms of bioactivity, the nanoceramics obtained and presented in this work reveal attractive and varied morphological and structural properties. Therefore, they may find a potential application as a biomaterial in bone tissue repair or as a buffer layer prepared by the sol-gel method. Further studies related to the use of other synthesis procedures and techniques as well as other dopants concentrations are in progress.

Acknowledgments

This research was financed by the statutory funds of Faculty of Applied Physics and Mathematics, Gdansk University of Technology, Gdansk, Poland (Polish Ministry of Science and Higher Education Information no 5636/E-359/S/2018).

References

[1] Best S.M., Porter A.E., Thian E.S., Huang J.: Bioceramics: Past, present and for the future. Journal of the European Ceramic Society 28 (2008) 1319-1327.
[2] Hong Y., Fan H., Li B., Guo B., Liu M., Zhang X.: Fabrication, biological effects, and medical applications of calcium phosphate nanoceramics. Materials Science and Engineering R 70 (2010) 225-242.
[3] Orlovskii V.P., Komlev V.S., Barinov S.M.: Hydroxyapatite and Hydroxyapatite-Based Ceramics. Inorganic Materials 38 (2002) 973-984.
[4] Fihri A., Len C., Varma R. S., Solhy A.: Hydroxyapatite: A review of syntheses, structure and applications in heterogeneous catalysis. Coordination Chemistry Reviews 347 (2017) 48-76.
[5] Ferraz M.P., Monteiro F.J., Manuel C.M.: Hydroxyapatite nanoparticles: A review of preparation methodologies. Journal of Applied Biomaterials & Biomechanics 2 (2004) 74-80.
[6] Samani S., Hossainalipour S.M., Tamizifar M., RezaieIn H.R.: In vitro antibacterial evaluation of sol-gel-derived Zn-, Ag-, and (Zn + Ag)-doped hydroxyapatite coatings against methicillin--resistant Staphylococcus aureus. Journal of Biomedical Materials Research Part A 101 (A) (2013) 222-230.
[7] Adzila S., Murad M.C., Sopyan I.: Doping Metal into Calcium Phosphate Phase for Better Performance of Bone Implant Materials. Recent Patents on Mater. Sci. 5 (2012) 18-47.
[8] Šupová M.: Substituted hydroxyapatites for biomedical applications: A review. Ceramics International 41 (2015) 9203-9231.
[9] Capanema N.S.V., Mansur A.A.P., Carvalho S.M., Silva A.R.P., Ciminelli V.S., Mansur H.S.: Niobium-Doped Hydroxyapatite Bioceramics: Synthesis, Characterization and In Vitro Cytocompatibility. Materials 8 (2015) 4191-4209.
[10] Maeda H., Lee S., Miyajima T., Obata A., Ueda K., Narushima T., Kasuga T.: Structure and physicochemical properties of CaO-P_2O_5-Nb_2O_5-Na_2O glasses. J. Non-Cryst. Solids 432 (2016) 60-64.
[11] Obata A., Takahashi Y., Miyajima T., Ueda K., Narushima T., Kasuga T.: Effects of Niobium Ions Released from Calcium Phosphate Invert Glasses Containing Nb_2O_5 on Osteoblast-Like Cell Functions. ACS Applied Materials & Interfaces 4 (2012) 5684-5690.
[12] Wagner C.D., Riggs W.M., Davis L.E., Moulder J.F., Muilenberg G.E.: Handbook of X-ray Photoelectron Spectroscopy. Perkin-Elmer Corporation (1979).
[13] NIST X-ray Photoelectron Spectroscopy Database, NIST Standard Reference Database Number 20, National Institute of Standards and Technology, Gaithersburg MD, 20899 (2000) [accessed 2019 Jan 20]. https://srdata.nist.gov/xps/.
[14] CasaXPS: Processing Software for XPS, AES, SIMS and More. c2018 Casa Software Ltd [accessed 2019 Jan 20]. http://www.casaxps.com/.
[15] Berzina-Cimdina L., Borodajenko N.: Research of Calcium Phosphates Using Fourier Transform Infrared Spectroscopy, Infrared Spectroscopy - Materials Science, Engineering and Technology, Prof. Theophanides Theophile (Ed.). InTech (2012) 123-148.
[16] Li P., Ohtsuki C., Kokubo T.: The role of hydrated silica, titania and alumina in introducing apatite on implants. J. Biomed. Mater. Res. 28 (1994) 7-15.
[17] Özer N., Rubin M.D., Lampert C.M.: Optical and electrochemical characteristics of niobium oxide films prepared by sol-gel process and magnetron sputtering A comparison. Sol. Energy Mater. Sol. Cells 40 (1996) 285-296.
[18] Simon D., Perrin C., Baillif P.: Electron spectrometry study (ESCA) of niobium and its oxides. Application to the oxidation at high temperature and low oxygen pressure. C. R. Acad. Sci. Ser. C 283 (1976) 241-244.

DRUG-LOADED MESOPOROUS SILICA/CALCIUM PHOSPHATE COMPOSITES FOR BONE REGENERATION

Adrian Szewczyk, Adrianna Skwira, Magdalena Prokopowicz*

Department of Physical Chemistry,
Faculty of Pharmacy, Medical University of Gdańsk,
Hallera 107, 80-416 Gdańsk, Poland
*e-mail: magdalena.prokopowicz@gumed.edu.pl

Abstract

In this work, we obtained a mesoporous silica--calcium phosphate composite (MSi-CaP) in the form of spherical granules (pellets) loaded with cefazolin as a model antibiotic. First, the MSi-CaP composite was manufactured in the powder form via the sol-gel method using a soft template. The cefazolin was loaded into the MSi-CaP using the immersion method. The pellets were composed of MSi-CaP powders (both placebo and cefazolin-loaded) and excipients, such as microcrystalline cellulose and ethyl cellulose. The pellets were obtained in the laboratory scale using the wet-granulation, extrusion and spheronization method. The pellets proved satisfactory mechanical properties which allowed for further investigations (the drug release studies and the mineralization potential assay) without a risk of pellets cracking. The complete drug release from the pellets was observed after 12 h. The burst release of cefazolin from the pellets was reduced by 3 when compared to the burst release of cefazolin-loaded MSi-CaP powders (90 and 30% after 15 min of release studies, respectively). The pellets showed the mineralization potential in vitro, confirmed by the SEM-EDX and FTIR methods. After 60 days of the mineralization potential assay in the simulated body fluid, the examinations revealed that the whole surface of pellets was covered with the carbonated hydroxyapatite in accordance with the desired morphology.

Keywords: *mesoporous silica, calcium phosphate, hydroxyapatite, composites, drug delivery*

[Engineering of Biomaterials 150 (2019) 16-21]

Article presented at conference: IMPLANTS 2019, 28-29 June, Gdansk, Poland.

Introduction

Bacterial bone infections occur mainly in adults, usually secondary to open bone injuries, bone reconstructions or implant insertions, and thus are difficult to diagnose and treat [1,2]. Pathogenic changes and necrosis of bone tissue caused by a progressive bacterial infection can be observed via X-ray radiography only if 50-75% of a bone matrix has already been damaged [3]. In most cases a bone biopsy must be performed. In clinical practice, chronic bone inflammation caused by bacterial infection is treated surgically with the simultaneous implementation of antibiotic therapy [2,4]. The use of drug-loaded bone delivery systems (bone fillers) is intended to replace dead tissue, reduce the risk of secondary infection and support bone regeneration [5,6]. Despite advances in surgery, biomaterials engineering, and pharmaceutical technology, bacterial bone infections can remain latent for many years after the treatment, with complete recurrence in 20-30% of patients.

For the last 20 years, bone regenerative medicine has been a promising multidisciplinary science which focuses on biomaterials for bone healing and replacement [5,7]. One of the most innovative strategies for treating bacterial bone infections is the application of bifunctional biomaterials which assure the drug delivery directly into the infected area and support bone regeneration. Much attention is paid to biomaterials which support the damaged bone tissue thanks to the efficient mechanical and biological properties. Among them, mesoporous silica-calcium phosphate composites are investigated [8,9]. Mesoporous silicas are characterized by the high surface area, uniform pore size (4-10 nm), high surface area to volume ratio, modifiable particles shape, and high thermal resistance. Due to these properties, they are studied as drug carriers [10,11]. On the other hand, calcium phosphates, especially hydroxyapatite, are known as excellent bone regenerating biomaterials due to their high biocompatibility and osteoconductivity [12,13]. The calcium phosphates exhibit good biological stability and affinity to bone as they convert into the carbonated hydroxyapatite after implantation. In terms of the composition and structure, the carbonated hydroxyapatite is equivalent to the mineral bone matrix [13,14].

Unfortunately, due to the small particle size of mesoporous silica/calcium phosphate composites, their porosity, low bulk density and adhesion, these materials cannot be directly manufactured in the pharmaceutical technology and biomaterials engineering processes. Only the addition of excipients, the use of appropriate equipment and the proper validation of the manufacturing process makes it possible to obtain a bifunctional drug delivery system for bone regeneration based on mesoporous silica/calcium phosphate composites.

In this work, we obtained the mesoporous silica/calcium phosphate composites formed as pellets loaded with cefazolin as a model antibiotic used to treat bacterial bone infections. The term “pellets” refers to small (approx. 1 mm), free-flowing, spherical granules manufactured by the agglomeration of fine powders via the wet-granulation, extrusion, and spheronization process. The obtained pellets were subjected to the mechanical properties examinations (hardness test, friability test), drug release studies and mineralization potential *in vitro* defined as a possibility to form the hydroxyapatite layer on the surface of the pellets immersed in the simulated body fluid.

Materials and Methods

The mesoporous silica/calcium phosphate composites (MSi-CaP) were synthesized using the sol-gel method [15]. The tetraethyl orthosilicate (TEOS) and cetyltrimethylammonium bromide (CTAB) were used as a silica precursor and a structure directing agent, respectively. The calcium chloride anhydrous ($CaCl_2$) and potassium dihydrogen phosphate (KH_2PO_4) were applied as calcium phosphate precursors. All reagents were purchased from Sigma-Aldrich. The synthesis was carried out in an aqueous media with the addition of absolute ethanol and 25 wt% ammonia. The corresponding molar ratio of reagents TEOS:CTAB:$CaCl_2$:KH_2PO_4:water:ethanol:ammonia was 0.034:0.007:0.009:0.007:7.33:0.27:0.14. Briefly, water, ethanol, aqueous ammonia and CTAB were mixed in a polypropylene beaker for 15 min, at 300 rpm. The pH of the obtained solution was 10. Next, $CaCl_2$, K_2HPO_4, and TEOS were added and the resulting mixture was continuously stirred for 2 h.

Then the mixture was stored at 90°C for 5 days. The resulting solid product was recovered by the vacuum filtration, washed with 100 ml of absolute ethanol and dried at 40°C for 1 h. The CTAB template was removed from the product using calcination in the air (6 h at 550°C, heating rate of 1°C/min) in a muffle furnace (FCF 7MS series). The final powder composites were micronized in a grinder (Mortar Grinder Pulverisette 2, Fritsch) for 5 min at 75 rpm to obtain 200-500 μm fraction for further studies.

Cefazolin (Cef) was loaded into the composites using the immersion method. In brief, each sample of 200 mg of synthesized composites was immersed for 30 min in a concentrated (10 mg/mL) aqueous solution of cefazolin sodium (Biofazolin, Polpharma) while vigorously shaken. Next, the suspension was filtrated in a vacuum and the concentration of the cefazolin remaining in the solution was examined by monitoring the changes in absorbance at 271 nm by means of the UV-Vis spectrophotometer Shimadzu, (model UV-1800). The cefazolin-loaded composites were dried at room temperature for 24 h. The calculated mean amount of drug loaded into the composite was 32.9 ± 2.5 mg per 1 g of the composite.

Both the placebo mesoporous silica/calcium phosphate composites (MSi-CaP) and the ones loaded with cefazolin (MSi-CaP-Cef) were used to manufacture pellets via the granulation, extrusion and spheronization technique using Caleva Multi Lab apparatus (FIG. 1). The size of each batch was 5 g. Each formulation was composed of MSi-CaP, MSi-CaP-Cef and excipients: microcrystalline cellulose (MCC; Avicel PH 101, Sigma-Aldrich) and ethylcellulose (EC; Ethocel 20 cP, Dow Chemical) in the amounts of 30, 20, 45, 5 wt%, respectively. The powders were first premixed in a mortar and then in a granulator attachment (100 rpm, 5 min). The mass was wet-agglomerated using the EC ethanolic binder solution (5 wt%) in the same attachment (100 rpm, 5 min). The optimal volume of binder solution was determined using Caleva Torque Rheometer. The wet mass was then extruded in an extruder attachment running at 100 rpm with a circular 1 mm holes diameter and depth. The entire batch of the extrudate was then spheronized in a spheronizer attachment of 8.5 cm in diameter (2500 rpm, 5 min). The resultant pellets were left to dry overnight at room temperature. For further studies (drug release and mineralization potential studies) the main fraction of pellets (0.8-1.0 mm) was chosen as the fraction obtained from sieving with the highest weight (≥80%).

The drug release studies were performed using USP II Paddle Apparatus (Copley DIS-6000) at 37°C, 50 rpm. A constant fraction of the pellets was used for each batch. Purified water (pH=7.0; 500 mL) was applied as a dissolution media providing sink conditions. At suitable time intervals, 2.0 mL of solutions were filtered using membrane filters (0.45 μm) and analyzed spectrophotometrically at 271 nm. The drug stability was provided during the whole release studies. The drug release data were plotted as the cumulative percent of Cef released (Q) as a function of time (t). The release studies were repeated 6 times. The same release studies were carried out for the parent MSi-CaP-Cef powders for comparative purposes.

The mineralization potential assay of the pellets was carried out in the simulated body fluid (SBF) [16]. Each 200 mg of pellets was soaked in 100 mL of SBF in polypropylene containers. The samples were stored in a water bath for 60 days (37°C, 70 rpm). The SBF was exchanged for the fresh one every 24 h.

The composites were investigated using Fourier Transform Infrared Spectroscopy (FTIR, Jasco model 410, KBr technique, 4 cm^{-1} resolution with spectra standardization to maximum absorbance at ~1080 cm^{-1} peak), the scanning electron microscopy equipped with energy dispersive X-ray spectroscopy (SEM-EDX, Hitachi SU-70, samples were gold-coated), transmission electron microscopy (TEM, Tecnai G2 T20 X-TWIN) and stereoscopic microscope (Opta-TECH X 2000). The hardness (referred to as a force at 90% strain) and friability of the pellets were tested using texture analyzer (TA.XT plus, granule compaction rig) and friabilator (Erweka TAR 10, 4 min, 25 rpm), respectively.

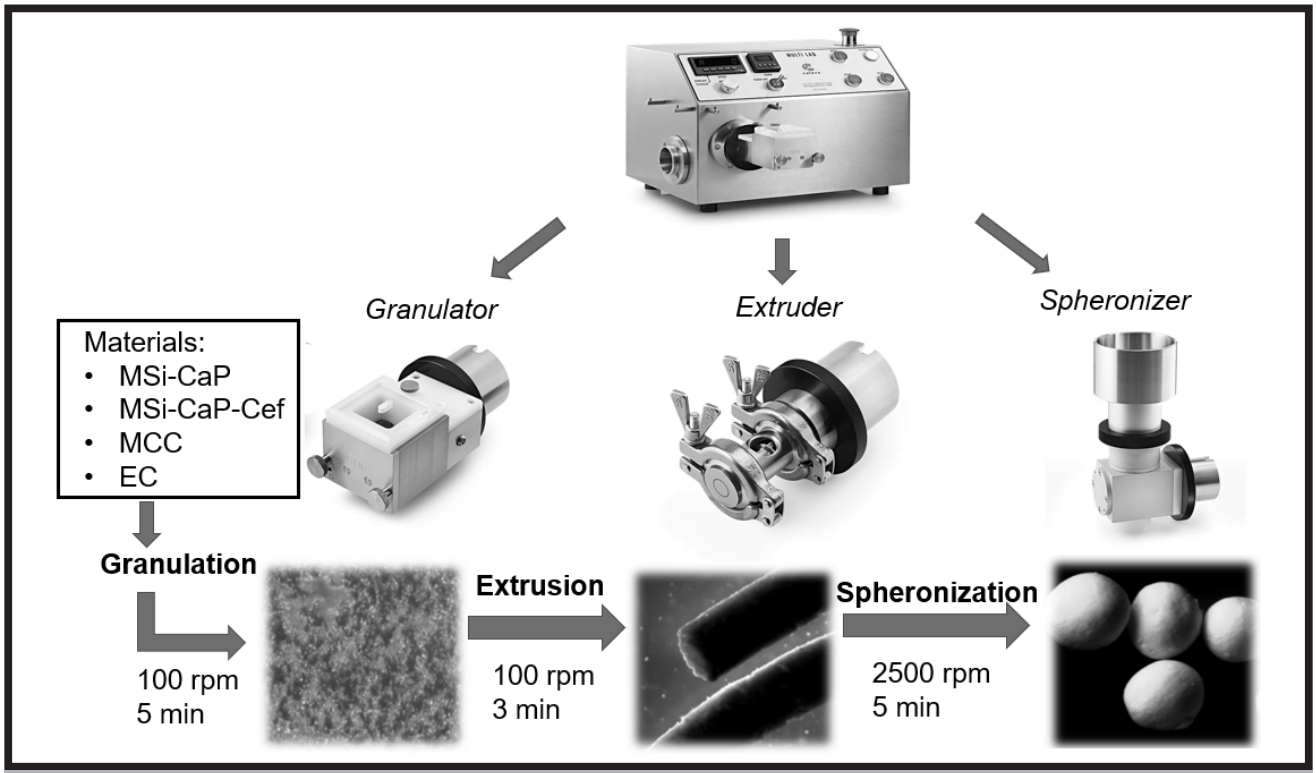

FIG. 1. The schematic illustration of pelletization process for the mesoporous silica-calcium phosphate composites.

Results and Discussions

The SEM and TEM micrographs of MSi-CaP-Cef composite are presented in FIG. 2. Both the SEM (FIG. 2a) and TEM (FIG. 2b) results showed the biphasic nature of the obtained composites: spherical drug-loaded silica particles and rod-like calcium phosphate precipitates. As presented in FIG. 2c, the silica particles were characterized by mesoporous structure (~3.5 nm pore diameter), typical for silica materials obtained via the sol-gel method with CTAB as a structure directing agent [17,18].

The FTIR spectra of both the parent and Cef-loaded MSi-CaP powders and pellets are presented in FIG. 3. In the FTIR spectrum of parent MSi-CaP composite (FIG. 3, left) the bands characteristic for silica (1090, 960, 800, 465 cm^{-1} of ν_{as} Si-O-Si; ν_{β} Si-OH; ν_{s} Si-O and δ O-Si-O vibrational modes, repetitively) [19] and phosphates (604, 565 cm^{-1} assigned to ν_4 vibrational mode of P-O-P in $(PO_4)^{3-}$ group) [20] were observed, which also confirmed the biphasic nature of synthesized material. In the case of Cef-loaded composite (MSi-CaP-Cef) (FIG. 3, left) the bands characteristic for Cef molecule confirmed the drug presence in the MSi-CaP composite after the loading procedure. The shift in bands from 1759 to 1761 cm^{-1} and from 1357 to 1363 cm^{-1} may suggest the weak chemical interaction via hydrogen bonding between Cef molecules and the MSi-CaP surface.

The chemical interactions between silanols present on the silica surface and Cef molecules are a well-known phenomenon [21]. It has been reported that the silanols present on the mesoporous silica surface are characterized by pKa approx. 8 and 2 for geminal (Q_2, $=Si(OH)_2$) and free (Q_3, $\equiv SiOH$) silanols, respectively [22]. Under the provided adsorption conditions (10 mg/mL cefazolin sodium aqueous solution, pH=4.5, room temperature) both CEF molecules and free silanols ($\equiv SiOH \rightleftarrows SiO^- + H^+$) were negatively charged, whereas the geminal silanols were undissociated. Thus, the electrostatic repulsion and hydrogen bonding between silica surface and CEF might influence the adsorption process. However, it is worth mentioning that the adsorption of CEF onto the mesoporous silica was primarily characterized as physical in nature [21]. The FTIR spectrum of final MSi-CaP-Cef pellet (FIG. 3, right) reveals bands characteristic for Cef-loaded MSi-CaP composite (1762, 1083, 800, 604, 562, 463 cm^{-1}) and excipients used in pelletization process: microcrystalline cellulose and ethyl cellulose (2975, 2903, 1376, 660 cm^{-1} of C-H stretching, C-H stretching, C-H bending and C-OH bending vibrations, respectively) [23].

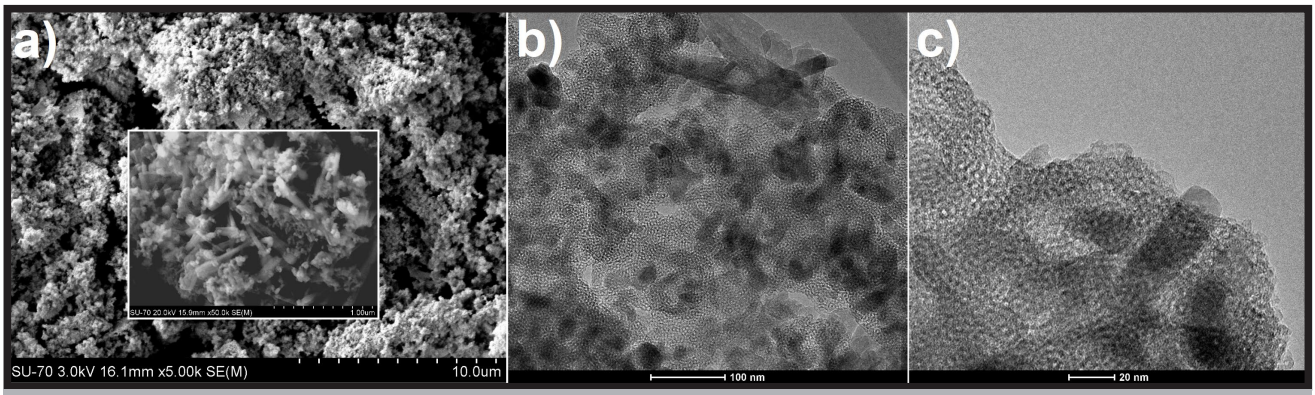

FIG. 2. The SEM (a) and TEM (b,c) micrographs of the obtained MSi-CaP-Cef composites.

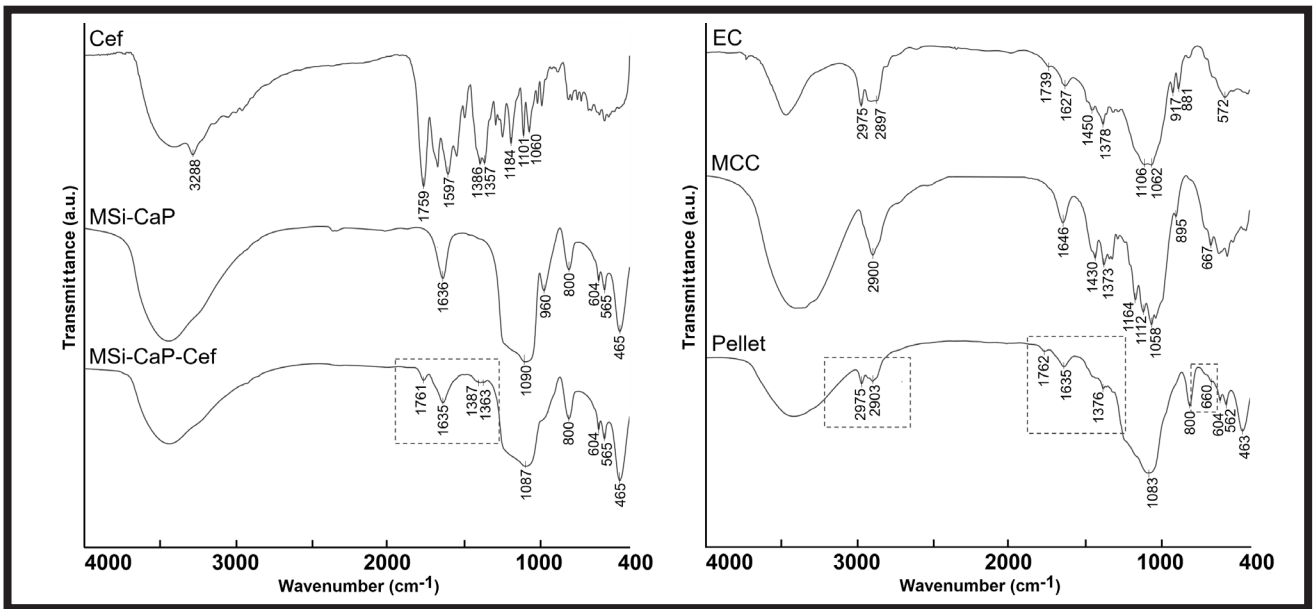

FIG. 3. The FTIR spectra of the MSi-CaP composite before and after Cef loading with the Cef reference sample (left) and the obtained pellet with the EC and MCC reference samples (right).

TABLE 1. The hardness and friability values of the MSi-CaP-Cef pellets.

Batch number	Force at 90% strain (g)	Mean ± SD (g)	Friability (%)	Mean ± SD (%)
1	58.3	59.0 ± 4.3	2.1	2.3 ± 0.3
2	64.5		2.7	
3	54.1		2.2	

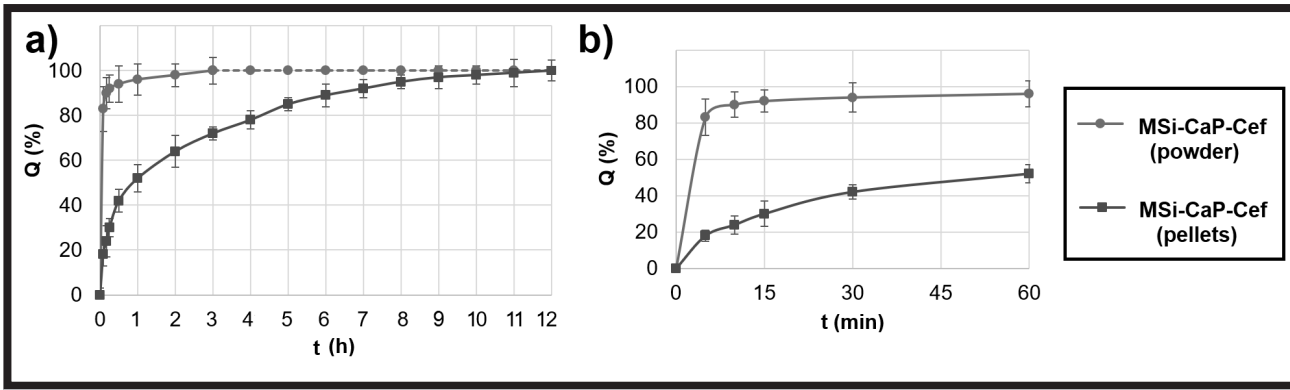

FIG. 4. The cefazolin release profiles (a) and burst release stage (b) of the MSi-CaP-Cef powders and pellets.

The hardness and friability of the CaP-MSi-Cef pellets are presented in TABLE 1. The mean force at 90% strain was 59.0 ± 4.3 g, whereas the mean friability was 2.3 ± 0.3. The similar results obtained for 3 independent batches confirmed the repeatability of the pelletization process. The obtained mechanical properties provided the pellets stability during the drug release studies and mineralization potential assay. The pellets did not disintegrate and stayed completely spherical after 60 days of incubation in SBF.

The drug release profiles of MSi-CaP-Cef composites in the form of powders and pellets are presented in FIG. 4. For the MSi-CaP-Cef powders the complete drug release was achieved after 3 h of studies (FIG. 4a) and it was preceded by high burst release – almost 90 ± 6% of Cef was released during the first 15 min. It might suggest that chemical interactions between Cef molecules and the MSi-CaP composite surface were weak and did not have an important impact on the release profile. It should be noticed that both Cef molecules and silica surface are negatively charged under the performed conditions of drug release studies, so the electrostatic repulsion between those specimens might occur, increasing the burst stage [21]. Although the hydrogen bonding between Cef and the silica surface seems to be sufficient for drug loading, it cannot compensate for a relatively stronger electrostatic repulsion during the drug release. Thus, the high burst release is observed for the MSi-CaP-Cef powders. For the MSi-CaP-Cef composites shaped as pellets the complete drug release was observed after 12 h of studies (FIG. 4a) with a significantly slowed down burst stage (FIG. 4b) – the amount of Cef released after 15 min was reduced by 3 (from 90 ± 6% to 32 ± 5% for the powders and pellets, respectively). The prolonged release of the drug from the pellets can be explained as follows. The manufactured pellets had a much smaller surface area as compared to powders, thus the effective surface area available for water to dissolve the drug was significantly reduced. Moreover, the penetration of water into the pellets was impeded due to the presence of hydrophobic excipients: MCC and EC. The used excipients acted as a hydrophobic boundary which limited the access of water to drug molecules inside the matrix and consequently extended the diffusion path length [24]. The obtained pellets were characterized by a relatively fast (12 h) and complete CEF release as compared to other bone implants (>30 days) [25]. The fast drug release may ensure the high local concentration of antibiotics immediately after the orthopaedic surgery, thus reducing the dosage of parenteral antibiotics and the risk of side effects during the pharmacological treatment. Moreover, the complete drug release from the proposed MSi-CaP-Cef pellets seems to be an important feature of bone drug delivery systems preventing antibiotic resistance. In contrast, the commonly used bone cements are characterized by the incomplete and sustained release of loaded antibiotics causing the local sub-inhibitory concentrations in the infected bone that increase the risk of antibiotic resistance [26,27].

The SEM micrographs with corresponding EDX profiles for the MSi-CaP-Cef pellets before and after 60 days of mineralization potential assay in SBF are presented in FIG. 5. The primary pellets were characterized by a smooth surface composed of two domains: the MSi-CaP-Cef domain in the form of semi-spherical particles or rods (high Si, Ca, P content in EDX profile) and the MCC-EC domain in the form of elongated strands (high C, O content in EDX profile). The observed sulphur in the EDX profile no. 1 (FIG. 5, top) derived from the Cef molecules loaded into the MSi-CaP composites. After 60 days of mineralization assay, the surface of the pellets became rough with small (100-150 μm length) cracks as a consequence of SBF penetration into the pellets matrix. The whole surface of pellets was covered by the needle-like and flower-shaped continuous layer. According to the EDX profile no. 2 (FIG. 5, bottom), the morphology of precipitate and our previous results [28], such a layer might be considered as the carbonated hydroxyapatite. However, it was also observed that some MCC-EC domains were not covered by the hydroxyapatite layer due to their weaker mineralization potential if compared to the MSi-CaP composite, which was confirmed by the EDX no. 1 (FIG. 5, bottom). The possible mechanism of carbonated hydroxyapatite formation on the pellets surface might be connected with the presence of calcium phosphate in the MSi-CaP composite.

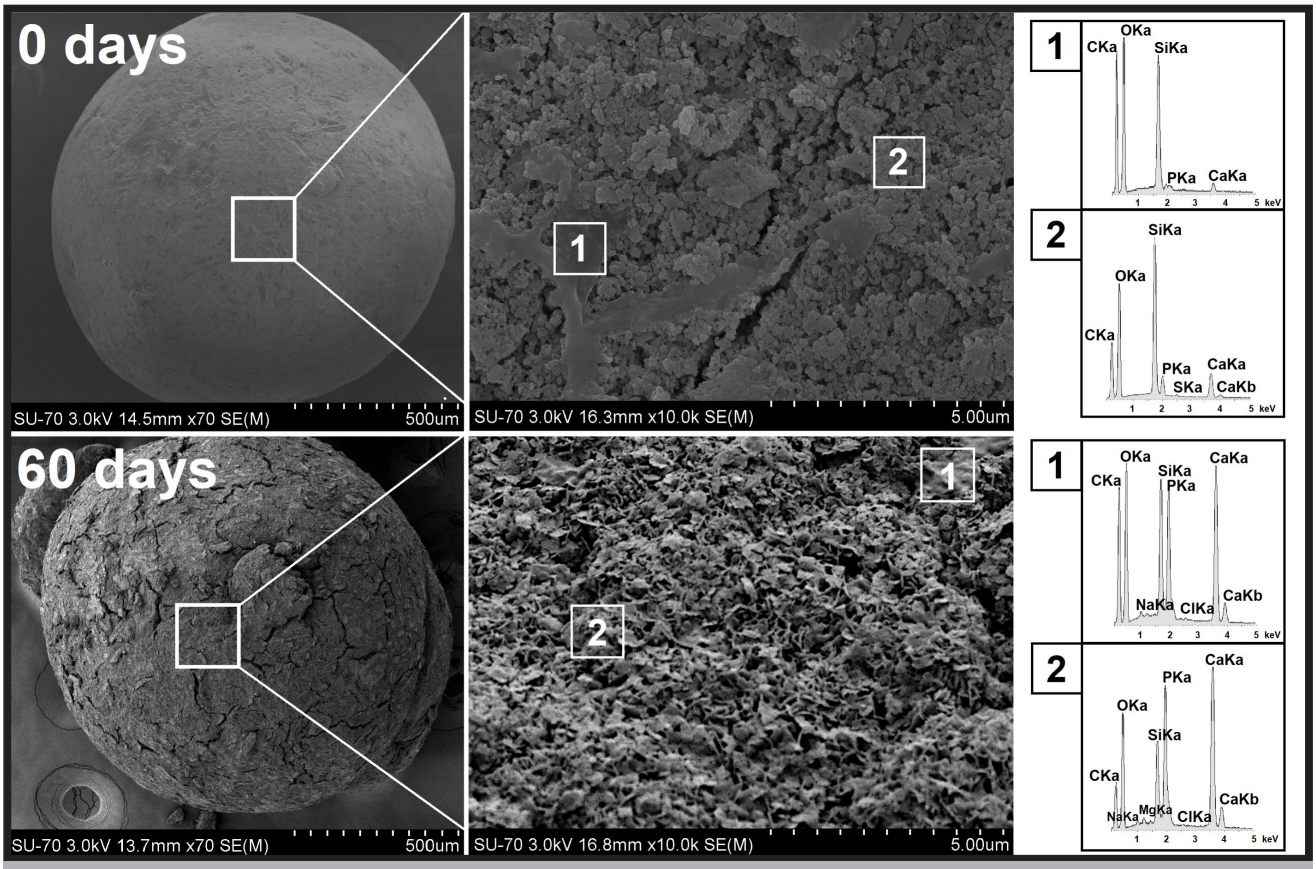

FIG. 5. The SEM micrographs with corresponding EDX profiles of the MSi-CaP-Cef pellets before and after 60 days of the mineralization assay in SBF.

Such a calcium phosphate may act as a metastable form which has partially dissolved in the SBF and precipitated on the surface of the pellets as the stable hydroxyapatite form. The precipitated hydroxyapatite nuclei absorb accessible calcium and phosphate ions from the SBF in order to form aggregates, clusters and continuous layers. The spreading of hydroxyapatite on the whole surface of the pellets was most probably promoted by the silanol groups of mesoporous silica which, in turn, facilitated the further formation of new hydroxyapatite nucleation centers. As it is presented in the EDX profile no. 2 (FIG. 5, bottom), the magnesium, sodium and carbonate ions were incorporated into the hydroxyapatite structure proving the dynamic nature of the apatite formation process. The Ca/P molar ratio of the formed hydroxyapatite was 1.71 (data not shown), thus similar to the human bone apatite.

The progressive formation of carbonated hydroxyapatite was also confirmed by the FTIR results (FIG. 6). The shift in the absorbance of the maximum peak from 1087 to 1092 cm^{-1} might be observed due to the increasing intensity of v_3 $(PO_4)^{3-}$ vibrational modes [29]. Moreover, after 60 days of the mineralization potential assay, the maximum absorbance peak divided into two: at 1092 and 1053 cm^{-1}, as a consequence of the increased P-O vibrations. The progressive increase of the peaks at 604, 562 cm^{-1} (v_4 of P-O-P) in the function of the SBF incubation time was also observed. The relative increase in the bands' intensity in the 1450-1430 cm^{-1} region may be connected with the carbonates incorporated into the hydroxyapatite structure (v_3 and C-O vibrational modes) [30].

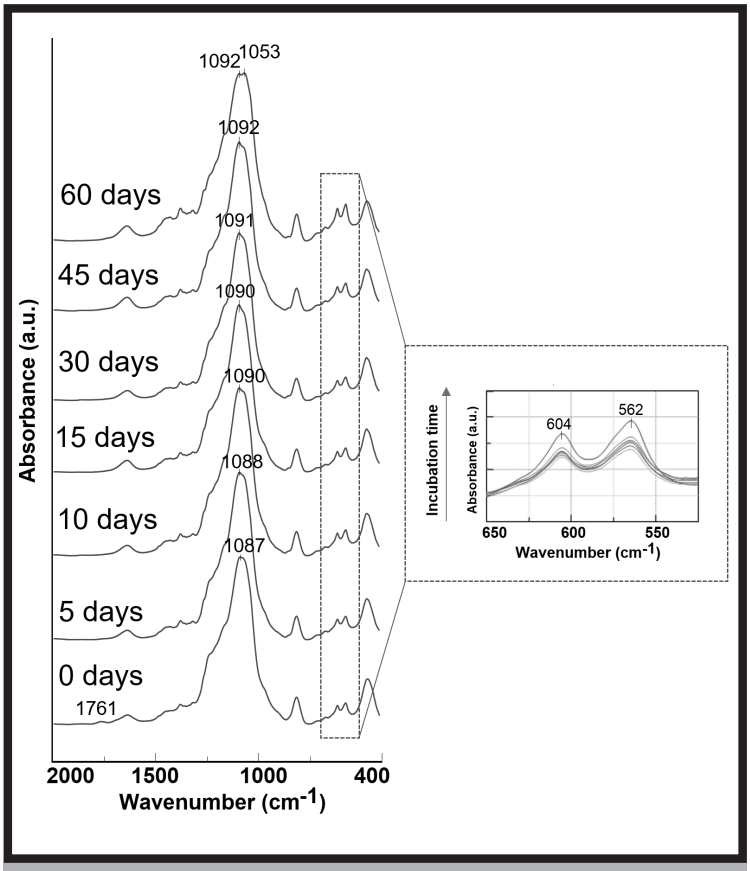

FIG. 6. The FTIR spectra of MSi-CaP-Cef pellets obtained during the mineralization potential assay in SBF.

Conclusions

The addition of calcium phosphate (CaP) precursors during the sol-gel process of mesoporous silica (MSi) synthesis allowed to obtain the biphasic MSi-CaP composites with preserved adsorption capacity. The cefazolin-loaded composites in the form of powders were suitable for the pelletization process, having added excipients. The obtained spherical granules (pellets) were characterized by the complete 12 h drug release and the surface hydroxyapatite formation after immersion in the simulated body fluid. The complete and relatively fast drug release from the pellets may support the pharmacological treatment of bacterial bone infections, immediately after the surgery. The obtained pellets require further studies (antimicrobial activity, cytotoxicity assay) to investigate their application potential in the fields of bone drug delivery systems.

Acknowledgments

This project was supported by the Polish National Science Centre (project OPUS 15 no. 2018/29/B/NZ7/00533) awarded to Magdalena Prokopowicz.

The study was supported by the project POWR.03.02.00-00-I026/17-00 co-financed by the European Union through the European Social Fund under the Operational Programme Knowledge Education Development 2014–2020.

References

[1] M.C. Birt, D.W. Anderson, E. Bruce Toby, J. Wang: Osteomyelitis: Recent advances in pathophysiology and therapeutic strategies, J. Orthop. 14 (2017) 45–52.
[2] N. Rao, B.H. Ziran, B.A. Lipsky: Treating Osteomyelitis: Antibiotics and Surgery, Plast. Reconstr. Surg. 127 (2011) 177S-187S.
[3] J. Calhoun, M.M. Manring, M. Shirtliff: Osteomyelitis of the long bones, Semin. Plast. Surg. 23 (2009) 059–072.
[4] A.L.L. Lima, P.R. Oliveira, V.C. Carvalho, S. Cimerman, E. Savio: Recommendations for the treatment of osteomyelitis, Brazilian J. Infect. Dis. 18 (2014) 526–534.
[5] M.R. Newman, D.S. Benoit: Local and targeted drug delivery for bone regeneration., Curr. Opin. Biotechnol. 40 (2016) 125–132.
[6] I. Izquierdo-Barba, L. Ruiz-González, J.C. Doadrio, J.M. González-Calbet, M. Vallet-Regí: Tissue regeneration: A new property of mesoporous materials, Solid State Sci. 7 (2005) 983–989.
[7] A. Oryan, S. Alidadi, A. Moshiri, N. Maffulli: Bone regenerative medicine: classic options, novel strategies, and future directions, J. Orthop. Surg. Res. 9 (2014) 18.
[8] M. Vallet-Regi, I. Izquierdo-Barba, M. Colilla: Structure and functionalization of mesoporous bioceramics for bone tissue regeneration and local drug delivery, Philos. Trans. R. Soc. A Math. Phys. Eng. Sci. 370 (2012) 1400–1421.
[9] C. Li, C. Jiang, Y. Deng, T. Li, N. Li, M. Peng, J. Wang: RhBMP-2 loaded 3D-printed mesoporous silica/calcium phosphate cement porous scaffolds with enhanced vascularization and osteogenesis properties, Sci. Rep. 7 (2017) 41331.
[10] C. Bharti, U. Nagaich, A.K. Pal, N. Gulati: Mesoporous silica nanoparticles in target drug delivery system: A review., Int. J. Pharm. Investig. 5 (2015) 124–33.
[11] J. Flynn, S. Mallen, E. Durack, P.M. O'Connor, S.P. Hudson: Mesoporous matrices for the delivery of the broad spectrum bacteriocin, nisin A, J. Colloid Interface Sci. 537 (2019) 396–406.
[12] V.S. Kattimani, S. Kondaka, K.P. Lingamaneni: Hydroxyapatite–Past, present, and future in bone regeneration, Bone Tissue Regen. Insights. 7 (2016) 9–19.
[13] D.K. Kim, S.J. Lee, T.H. Cho, P. Hui, M.S. Kwon, S.J. Hwang: Comparison of a synthetic bone substitute composed of carbonated apatite with an anorganic bovine xenograft in particulate forms in a canine maxillary augmentation model, Clin. Oral Implants Res. 21 (2010) 1334–1344.
[14] S. Tang, B. Tian, Q.F. Ke, Z.A. Zhu, Y.P. Guo: Gentamicin-loaded carbonated hydroxyapatite coatings with hierarchically porous structures: drug delivery properties, bactericidal properties and biocompatibility, RSC Adv. 4 (2014) 41500–41509.
[15] M. Prokopowicz, K. Czarnobaj, A. Szewczyk, W. Sawicki: Preparation and in vitro characterisation of bioactive mesoporous silica microparticles for drug delivery applications, Mater. Sci. Eng. C. 60 (2016) 7–18.
[16] T. Kokubo, H. Takadama: How useful is SBF in predicting in vivo bone bioactivity?, Biomaterials. 27 (2006) 2907–2915.
[17] J. Kecht, T. Bein: Oxidative removal of template molecules and organic functionalities in mesoporous silica nanoparticles by H_2O_2 treatment, Microporous Mesoporous Mater. 116 (2008) 123–130.
[18] H. Chen, Y. Wang: Preparation of MCM-41 with high thermal stability and complementary textural porosity, Ceram. Int. 28 (2002) 541–547.
[19] R. Al-Oweini, H. El-Rassy: Synthesis and characterization by FTIR spectroscopy of silica aerogels prepared using several $Si(OR)_4$ and $R''Si(OR')_3$ precursors, J. Mol. Struct. 919 (2009) 140–145.
[20] H. Ye, X.Y. Liu, H. Hong: Characterization of sintered titanium/hydroxyapatite biocomposite using FTIR spectroscopy, J. Mater. Sci. Mater. Med. 20 (2009) 843–850.
[21] A. Szewczyk, M. Prokopowicz, W. Sawicki, D. Majda, G. Walker: Aminopropyl-functionalized mesoporous silica SBA-15 as drug carrier for cefazolin: adsorption profiles, release studies, and mineralization potential, Microporous Mesoporous Mater. 274 (2019) 113–126.
[22] J.M. Rosenholm, T. Czuryszkiewicz, F. Kleitz, J.B. Rosenholm, M. Lindén: On the nature of the Bronsted acidic groups on native and functionalized mesoporous siliceous SBA-15 as studied by benzylamine adsorption from solution, Langmuir. 23 (2007) 4315–4323.
[23] M. Fan, D. Dai, B. Huang: Fourier Transform Infrared Spectroscopy for natural fibres, in: Salih Salih (Ed.), Fourier Transform - Mater. Anal., 1st ed., InTech, 2012: pp. 45–68. https://www.intechopen.com/books/fourier-transform-materials-analysis/fourier-transform-infrared-spectroscopy-for-natural-fibres (accessed May 29, 2019).
[24] M.A. Quadir, M.S. Rahman, M.Z. Karim, S. Akter, M.T. Bin Awkat, M.S. Reza: Evaluation of hydrophobic materials as matrices for controlled-release drug delivery. Pak. J. Pharm. Sci. 16 (2003) 17–28.
[25] S.K. Nandi, S. Bandyopadhyay, P. Das, I. Samanta, P. Mukherjee, S. Roy, B. Kundu: Understanding osteomyelitis and its treatment through local drug delivery system, Biotechnol. Adv. 34 (2016) 1305–1317.
[26] R. Dorati, A. DeTrizio, T. Modena, B. Conti, F. Benazzo, G. Gastaldi, I. Genta: Biodegradable scaffolds for bone regeneration combined with drug-delivery systems in osteomyelitis therapy, Pharmaceuticals. 10 (2017) 96.
[27] E.A. Masters, R.P. Trombetta, K.L. de Mesy Bentley, B.F. Boyce, A.L. Gill, S.R. Gill, K. Nishitani, M. Ishikawa, Y. Morita, H. Ito, S.N. Bello-Irizarry, M. Ninomiya, J.D. Brodell, C.C. Lee, S.P. Hao, I. Oh, C. Xie, H.A. Awad, J.L. Daiss, J.R. Owen, S.L. Kates, E.M. Schwarz, G. Muthukrishnan: Evolving concepts in bone infection: redefining "biofilm", "acute vs. chronic osteomyelitis", "the immune proteome" and "local antibiotic therapy," Bone Res. 7 (2019) 20.
[28] M. Prokopowicz, J. Żeglinski, A. Szewczyk, A. Skwira, G. Walker: Surface-activated fibre-like SBA-15 as drug carriers for bone diseases, AAPS PharmSciTech. 20 (2019) 17.
[29] G.M.L. Dalmônico, D.F. Silva, P.F. Franczak, N.H.A. Camargo, M.A. Rodríguez: Elaboration biphasic calcium phosphate nanostructured powders, Boletín La Soc. Española Cerámica y Vidr. 54 (2015) 37–43.
[30] Y. Zheng, X. Liu, Y. Ma, T. Huo, Y. Li, C. Pei: Controlled synthesis of hydroxyapatite microspheres with hierarchical structure and high cell viability, Mater. Lett. 195 (2017) 18–21.

TEMPERATURE BEHAVIOUR OF CERAMIC BIOCOMPOSITES INVESTIGATED VIA HOT-STAGE MICROSCOPY

Justyna Pawlik*, Katarzyna Cholewa-Kowalska

AGH University of Science and Technology,
Faculty of Materials Science and Ceramics,
Department of Glass Technology and
Amorphous Coatings,
Al. Mickiewicza 30, 30-059 Krakow, Poland
*e-mail: pawlikj@agh.edu.pl

Abstract

In this study, sol-gel bioactive glasses and β-TCP composites were investigated regarding their thermal behaviour, microstructure, and phase composition. Sol-gel bioactive glasses based on the CaO-SiO_2 -P_2O_5 system of either a high SiO_2 content (S2) or a high CaO content (A2) were mixed with the β-TCP at 25:75, 50:50 and 75:25 weight ratios. Basing on the HSM results, i.e. shrinkage curves, densification intervals and characteristic temperatures, the sintering temperatures of composites were indicated. Scanning electron microscopy and X-ray diffraction were used to determine the microstructure and phase composition of composites after sintering at selected temperatures, i.e. 1100°C and 1200°C. The SEM/EDX investigations proved the well-sintered and densified microstructure of the sintered composites. The chemistry of sol-gel bioactive glasses influenced both the thermal behaviour and the phase composition of the composites. The dominant phases for A2-β-TCP materials were α-TCP, pseudowollastonite and β-TCP, while for S2-β-TCP – cristobalite, β-TCP, and α-TCP. However, the content of each phase varied, depending on the A2 or S2 content in the composite composition. Hot-stage microscopy provides useful information for selecting optimal sintering temperature in order to obtain well--sintered and strengthened material. Moreover, by a carefully selected combination of sol-gel bioactive glasses and β-TCP it is possible to obtain the materials with favorable phase composition with regard to biological activity.

Keywords: *Hot-Stage Microscopy, sol-gel glasses, bioactive glasses, biocomposites, tricalcium phosphates, β-TCP, sintering*

[Engineering of Biomaterials 150 (2019) 22-28]

Introduction

Bioceramic materials, such as bioactive glasses, hydroxyapatite or tricalcium phosphates, are widely investigated as synthetic bone grafts, due to their high biocompatibility and bone integration. Among them, bioactive sol-gel glasses prove enhancement of bioactive and biological properties, due to the presence of specific surface areas and higher solubility than the molten ones [1-3]. However, these materials have some limitations in terms of their physico-chemical properties, due to their deficient thermal behaviour impairing their sintering ability and mechanical performance [4,5]. To overcome these disadvantages bioactive glasses are often combined with other biomaterials like hydroxyapatite [5-7], titanium dioxide [8], polycaprolactone or other polymers [9-11]. The osteoconductive properties of calcium phosphates (i.e. hydroxyapatite, β- and α-tricalcium phosphates) have led to their use as a promising material for bone tissue repair. It is worth noticing that most of nowadays synthetic bone substitutes are composites of CaP's and/or another phase (PLA, bioglass, etc.). Several reports show that bioactive glass and HA composites exhibit stronger biological activities and enhanced mechanical performance in comparison to pure HA [12-14]. During the temperature treatment (upon 1000°C) hydroxyapatite may decompose into β-TCP and α-TCP. Both of them are recognized as biocompatible and more soluble than HA. In fact the solubility can be described as: HA<β-TCP<α-TCP [15,16].

The majority of ceramic biomaterials is fabricated by the thermal processing, mainly in order to obtain a desirable material shape and also to improve their mechanical properties thanks to the increase in crystallinity [17,18]. Studies reveal that high crystallinity of 45S5 Bioglass® may delay the surface activity, both *in vitro* and *in vivo* [19,20]. On the other hand, resistance to degradation and mechanical strength of bioactive glasses can be improved by the controlled crystallization of the material [21]. Physical and chemical phenomena occurring in ceramics materials during temperature treatment can be observed *in situ*, via the hot-stage microscopy (HSM). In general, this research method is based on investigating the sample placed inside the furnace, maintaining the necessary temperature and the thermal environment, while it is in *situ* observed with an optical instrument. A great variety of heating microscopes have been designed and used in materials science nowadays. The wide range of instrument specifications and the possibility of additional parameters measurements (i.e. simultaneous X-ray diffraction, differential calorimetric analyses, mapping of surface temperature distribution) give the great possibility and flexibility for the different specimen investigations [22,23].

There are three main components of the hot-stage microscope: 1) the electric furnace with the specimen carriage; 2) the observation unit with the microscope and the recording device (video camera); 3) the light source. The scheme of the HSM used in this work is presented in FIG. 1.

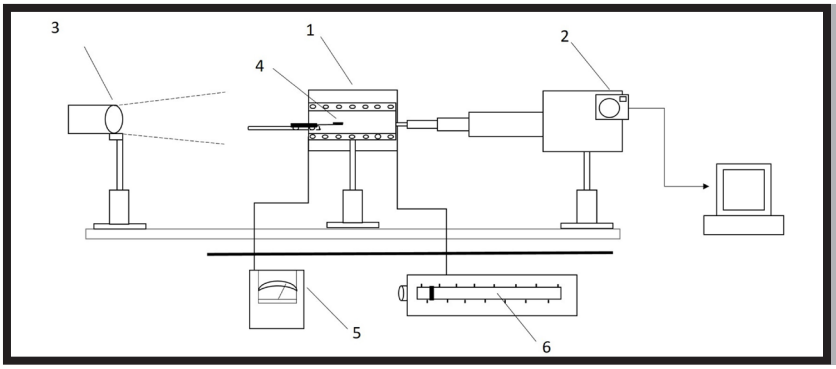

FIG. 1. Scheme of the hot-stage microscope:
1 - electric furnace,
2 - observation unit with the image/ video recording,
3 - light source,
4 - specimen and thermocouple,
5 - temperature controller,
6 - heating device.

The results of HSM investigations define the thermal behaviour of samples thanks to the specification of characteristic temperature values [23-25]:

- T_s - initial shrinkage temperature – when the melting begins on the contact points of the particular grains, while simultaneously the specimen size diminishes, but without changes of the initial shape,
- T_{sf} - softening temperature – when the first symptom of the specimen softening occurs with the visible shape changes, i.e. rounding off the cylinder corners of the specimen,
- T_m - melting temperature – when the specimen is melting, assuming the hemispherical form (generally established when hemisphere height equals approximately 2/3 of the initial specimen height),
- T_f - flowing temperature – when the specimen is flowing and forming a layer whose thickness is approximately equal to 1/3 of the specimen initial height.

The HSM results provide valuable data concerning not only the characteristic temperature values of the material (i.e. sintering softening, melting and flowing) but also its viscosity, wettability and surface tension [26-28]. This method is appropriate for examinations of glass, slags, ceramics, glazes and various raw materials by *real-time* observation and recording (photo capture or video record) how the sample contours change during the temperature increase [24]. Moreover, the most recent reports have proved that HSM is an effective method to investigate the thermal behaviour of biomaterials [29,30]. Hot stage microscopy was used to investigate new kinds of bioactive glass [29,31,32], bioglasses-based scaffolds [33,34] and ceramic-based biomaterials [35,36] in order to estimate their sintering ability. The usefulness of this method was proved in defining sintering routines and it stays in agreement with our previous investigations [5,37,38]. It is evident that a satisfactory balance of the biomaterial porosity/density and its mechanical strength is a key factor for biomaterials fabricated via thermal methods, as it affects their final physico-chemical properties and biological activity.

In this paper, we propose the application of the hot-stage microscopy to investigate biocomposites combined with the sol-gel bioactive glass (SBG) and β-TCP. These composites are intended as biomedical devices. We show here the practical use of HSM by examining composition of different composites (i.e. chemical composition of bioglass A2 - high lime glass, S2 - high silica glass and 25-75wt% of glass content in the composite) in order to evaluate their sintering temperatures necessary for materials processing. The major advantage of hot-stage microscopy is the possibility to determine the characteristic temperatures and thermal properties at the very early stage of the biomaterials designing, thus evaluating their usefulness. Further, in our work we present the results of composites sintered at selected temperatures along with the evaluation of their microstructure (SEM/EDX) and phase composition (XRD).

Materials and Methods

Two types of sol-gel bioactive glass (SBG) derived from the SiO_2-CaO-P_2O_5 system were synthesized as described previously [39,40]. They differed in chemical compositions and were designed as A2: 40SiO_2-54CaO-6P_2O_5 [%mol.] and S2: 80SiO_2-16CaO-4P_2O_5 [%mol.]. Summing up the process briefly, tetraethoxysilane (TEOS: $Si(OC_2H_5)_4$), triethylphosphate (TEP: $OP(OC_2H_5)_3$) and calcium nitrate tetra-hydrate ($Ca(NO_3)_2 \cdot 4H_2O$) were used as starting components in the sol-gel process. HCl solution was used as a catalyst for the hydrolysis and condensation reactions. The formed gel was dried in the oven at 800°C for 20 h and then milled and sieved to obtain a bioactive glass powder with particle sizes <45 μm.

Calcium phosphate – βTCP, purity ≥ 96.0% (CAS 7758-87-4) was purchased from Sigma-Aldrich, Germany.

Two types of sol-gel bioactive glass - S2 or A2 - were used to fabricate composites with β-TCP in the weight ratio of 25:75, 50:50 and 75:25. Pure A2, S2, and β-TCP materials were used as reference samples. Mixed and homogenized powders were used to prepare pellets (of 10 mm diameter) by uniaxial pressure at 100 MPa. Based on the HSM results - depending on the composites composition - the sintering temperature was 1100°C (S2-βTCP and the reference materials: S2, βTCP) or 1200°C (A2-βTCP and the reference sample A2). The heating rate was 5°C/min and the samples were held at the sintering temperature for 2 h and then cooled inside the furnace.

Hot-stage microscopy

The temperature behaviour and sintering ability of the SBG-β-TCP samples and reference ones were investigated by the hot-stage microscope (Leitz Wetzlar, Germany). The tests were performed in air using a heating rate schedule of 10°C/min between the 20°C and 1400°C. The mixed and homogenized powders were manually pressed into a cylindrical shape (3 x 3 mm). The compacted sample placed on the ceramic holder was inserted into the furnace at the room temperature and then the heating process started. The test proceeded until the temperature reached 1400°C or the flowing temperature of the sample was reached. While being heated the samples were observed with the video camera (magnification 20x) and thus the images of the changing sample profiles were acquired (FIG. 2). The potential systematic error occurrence was minimized by analyzing 3 samples of each material. Therefore, presented herein results of HM were described as mean ± standard deviation. The sample shrinkage at different temperatures (TABLE 1, FIG. 2) was calculated from the variation of the sample area, applying the following formula:

$$\text{Shrinkage (\%)} = (A_T/A_0) \times 100$$

where:
A_T – area of the sample at the temperature T [mm^2],
A_0 – initial area of the sample at room temperature [mm^2].

Scanning electron microscopy

The scanning electron microscopy (SEM) and energy dispersive X-ray analysis (EDX) (NOVA 200, NanoSEM, FEI, USA) were used to characterize the microstructure of the samples sintered at selected temperatures, i.e. 1100°C and 1200°C. The samples were sputtered with a thin layer of carbon and images were taken (mag. 1000x) at an operation voltage of 18 kV. The presented results are representative for each sample, yet several SEM/EDX analyses of different areas of each material were performed (FIG. 4).

X-ray diffraction

The phase composition of the heat-treated samples was studied by X-ray diffraction analysis (Philips X'Pert Pro MD) and the XRD patterns of the SBG-β-TCP composites and the reference materials are presented in FIG. 5. The phase identification was carried out by means of the PANalytical X'Pert HighScore Plus software.

Results and Discussions

Hot-stage microscopy was used to evaluate the thermal behaviour of SBG-β-TCP composites and reference samples (S2, A2, and β-TCP). The variations of samples shrinkage depending on the temperature are showed in FIG. 2. The thermal behaviour of composites followed the multi-stage shrinkage (densification) process characteristic for composite materials. However, the temperatures of each stage of densification varied depending on the composites composition and mostly were characterized by the temperature interval T_1-T_2 and T_3-T_4 (FIG. 2). Generally, the A2 glass samples were more thermally stable and the first stage of densification for the A2-β-TCP composites ranging from 1100-1270°C, while for the S2-β-TCP materials the first shrinkage temperature varied from 980-1150°C. The second stage of densification for the S2 glass composites was observed between 1110-1200°C. However, with the increasing temperature, the dimensions of the S2-β-TCP samples remained unchanged until the end of the test and the plateau of shrinkage curves for these samples was observed. This observation corresponds to the thermal curve for pure S2-sample. However, in this case, the only shrinking occurred at the lower temperature (780-800°C) and, despite heating, the material maintained its unchanged dimensions (plateau). This phenomenon can be correlated with the crystallization process when the viscosity increases and the viscous flow sintering is inhibited. For the A2 composites the temperature values of the second shrinkage stage were higher when compared to the S2-β-TCP samples, from 1280-1350°C. Moreover, with the increase in temperature, the samples dimensions decreased continuously. This may be attributed to the rapid reduction of the samples shape caused by increased softness and rapid decrease in viscosity, probably resulting from sintering with the liquid phase. The gratest shrinkage was observed for the A2-β-TCP composites (62-75%), while the S2-β-TCP composite revealed the shrinkage range from 82 to 94% (TABLE 1). These differences correlate with the type of glass (A2 or S2) in the composite composition, with the shrinkage of 64% and 86%, respectively.

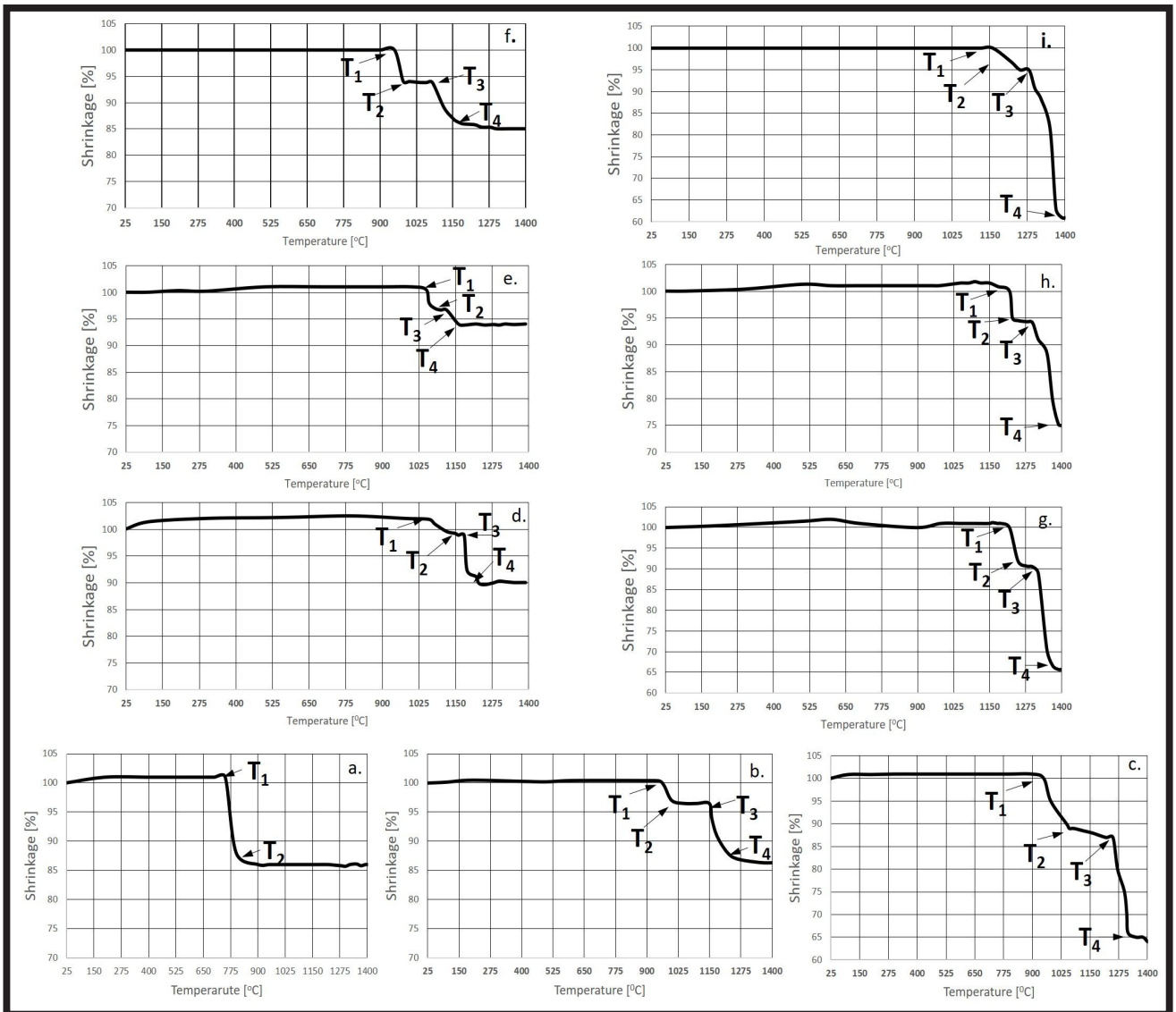

FIG. 2. Shrinkage curves derived from the HSM as a function of temperature for SBG-β-TCP composites and reference materials. Where: a. - S2, b. - β-TCP, c. - A2, d. - 25S2-β-TCP, e. - 50S2-β-TCP, f. - 75S2-β-TCP, g. - 25A2- β-TCP, h. - 50A2- β-TCP, i. - 75A2-β-TCP.
T_1, T_2 - temperature at the beginning and the end of the first densification stage,
T_3, T_4 - temperatures at the beginning and the end of the second densification stage.

TABLE 1. Characteristics of SBG-β-TCP composites and reference materials (A2, S2, β-TCP).

Sample	Shrinkage* [%]	Densification intervals* [°C]		Sintering temperature [°C]	Apparent density** [g/cm^3]
		T_1-T_2	T_3-T_4		
25A2-β-TCP	65.1 ± 0.2	1270-1300°C (ΔT = 30)	1350-1370°C (ΔT = 20)	1200	2.01 ± 0.12
50A2-β-TCP	75.0 ± 1.2	1230-1280°C (ΔT = 50)	1320-1390°C (ΔT = 70)	1200	1.69 ± 0.05
75A2-β-TCP	62.2 ± 0.3	1210-1250°C (ΔT = 40)	1310-1370°C (ΔT = 60)	1200	1.61 ± 0.07
25S2-β-TCP	90.1 ± 0.2	1120-1160°C (ΔT = 40)	1200-1280°C (ΔT = 80)	1100	2.46 ± 0.04
50S2-β-TCP	94.5 ± 1.1	1060-1100°C (ΔT = 40)	1160-1210°C (ΔT = 50)	1100	2.03 ± 0.06
75S2-β-TCP	82.1 ± 0.4	980-1020°C (ΔT = 40)	1120-1160°C (ΔT = 40)	1100	1.74 ± 0.02
A2	64.3 ± 0.5	980-1050°C (ΔT = 25)	1260-1310°C (ΔT = 50)	1200	1.71 ± 0.04
S2	86.0 ± 0.2	780-850°C (ΔT = 70)	-	1100	1.55 ± 0.03
β-TCP	86.3 ± 0.2	970-1050°C (ΔT =80)	1180-1220°C (ΔT = 40)	1100	2.23 ± 0.10

* based on the hot-stage microscopy results
** apparent density of samples after sintering at the selected temperature

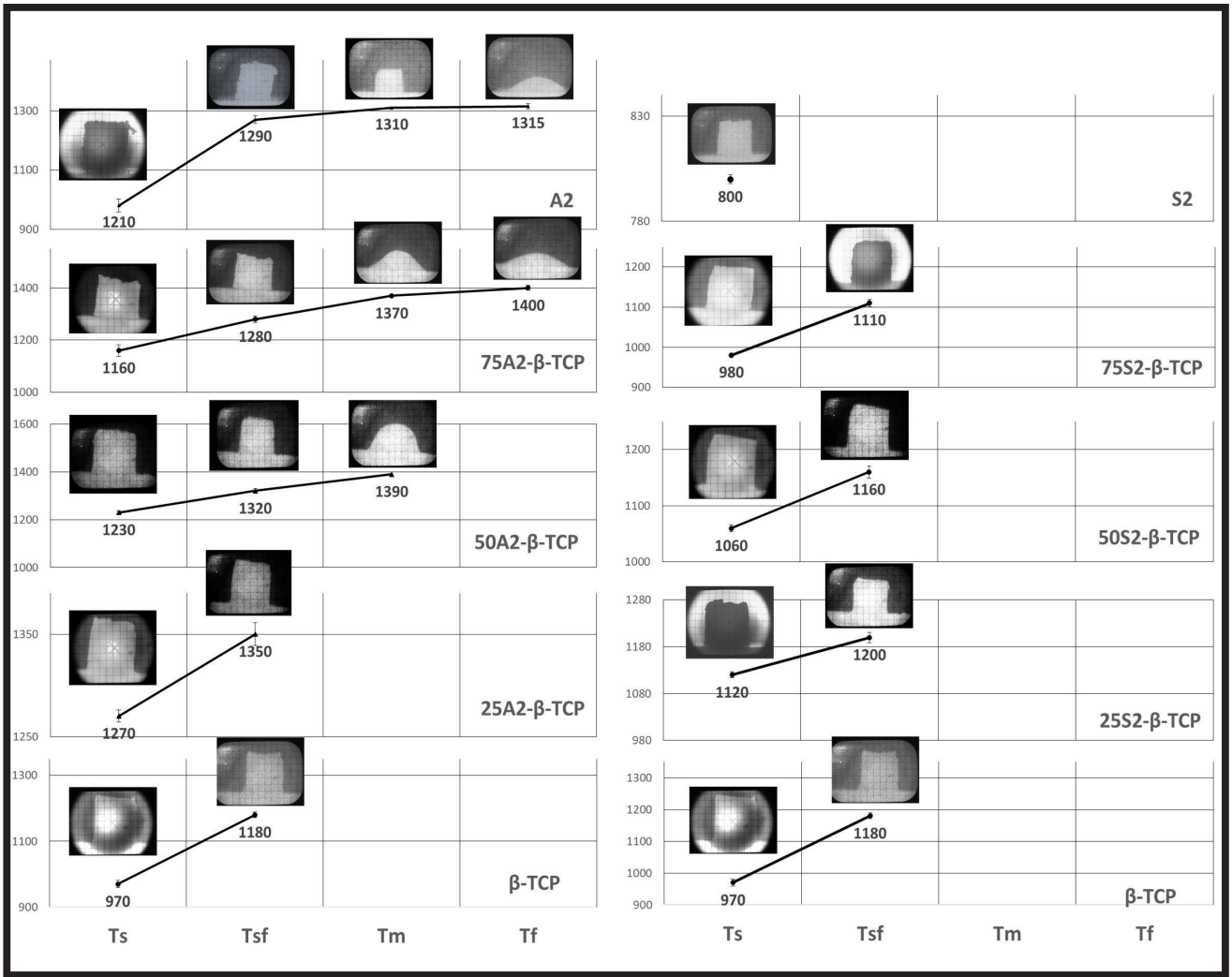

FIG. 3. The characteristic temperatures with correlated HTM images for A2-β-TCP, S2-β-TCP composites and reference sample (β-TCP, A2, S2). Where: T_s - initial shrinkage temperature, T_{sf} - softening temperature, T_m - melting temperature, T_f - flowing temperature.

Selecting the sintering temperatures of composites is a key step during the fabrication process. The hot-stage microscopy provides useful information how to accomplish this task. Basing on the shrinkage curves, the densification intervals and the *in situ* observation during HSM measurements the characteristic temperatures (i.e. T_s - initial shrinkage temperature, T_{sf} - softening temperature, T_m - melting temperature, T_f - flowing temperature) of the materials were selected. The results are presented in FIG. 3. A significant correspondence between the values of characteristic temperatures and the composition of composites can be observed:

- The addition of β-TCP to the composite composition influenced the increase in the characteristic temperatures in comparison with the addition of glass A2 or S2.
- The type of bioactive glass, i.e. A2 or S2, determines the values of characteristic temperatures, thus A2-β-TCP composites presented generally higher T_s and T_{st} than the S2-β-TCP materials.
- Both types of composites, i.e. A2-β-TCP and S2-β-TCP, showed the decrease in characteristic temperatures values with the increasing bioactive glass content.
- Only for the composites with 50 and 75wt% of A2 glass addition, the melting temperatures were visible, and the latter also revealed the flowing temperature, while negligible changes of the sample dimensions were observed for other materials beyond the sintering temperature.

As mentioned before, the results of hot-stage microscopy tests and *in-situ* observations of the sample profile during the measurements provide useful information for selecting the optimal sintering temperature to fabricate ceramic composites. This is a key parameter for obtaining the well densified and thus strengthened material with high biological activity provided by means of the phase composition. Therefore, the sintering temperatures for such glass-ceramic composites are usually considered between the T_s (initial shrinkage temperature) and T_{sf} (softening temperature). Based on the results of hot stage microscopy, the sintering temperatures of the SBG- β-TCP and the reference materials were selected as follows: 1100°C (β-TCP, S2, S2-β-TCP) and 1200°C (A2, A2-β-TCP) (TABLE 1).

The microstructure of the sintered SBG-β-TCP composites investigated by the SEM/EDX is presented in FIG. 4.

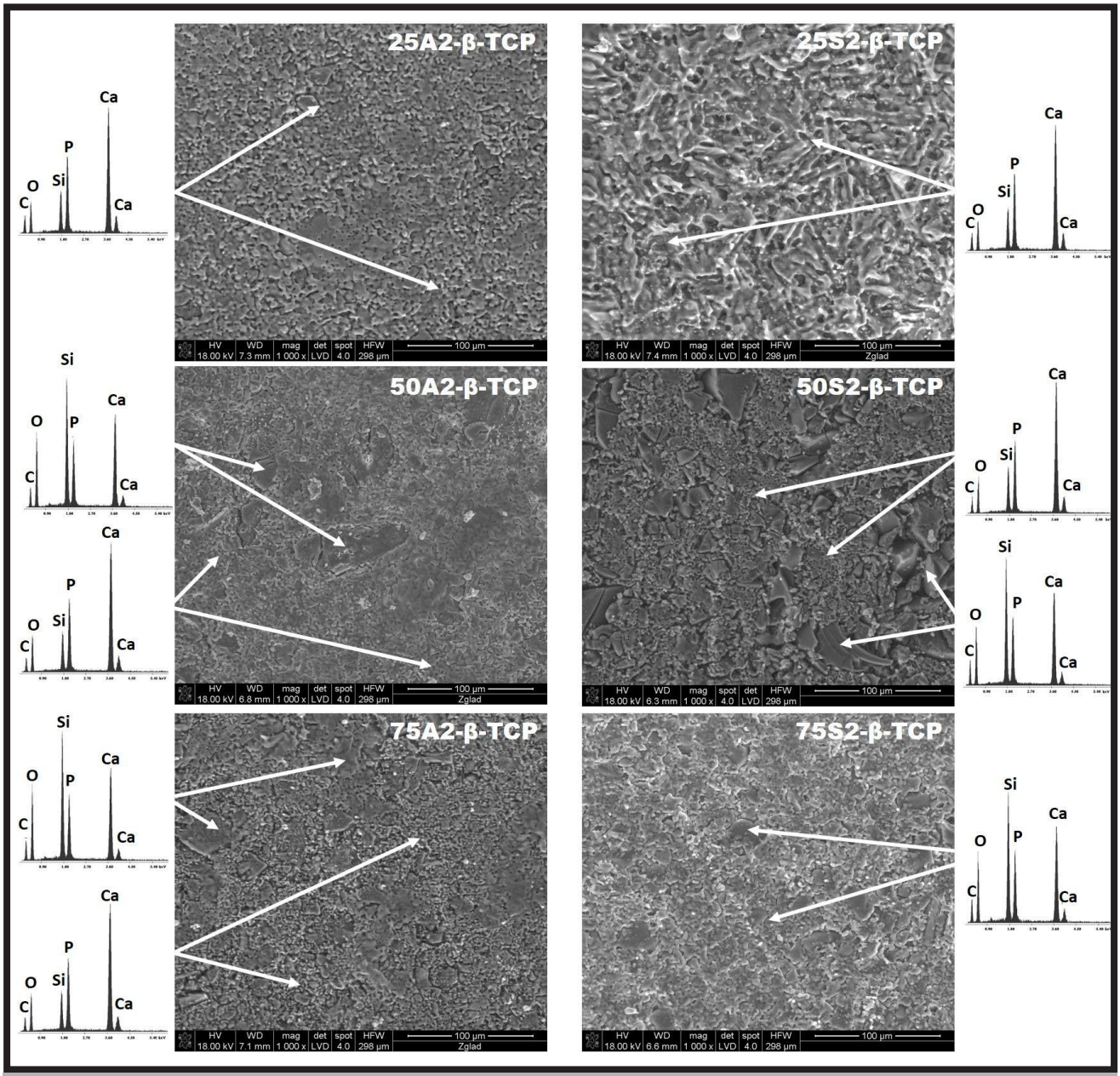

FIG. 4. SEM pictures and EDX spectra of SBG-βTCP composites.

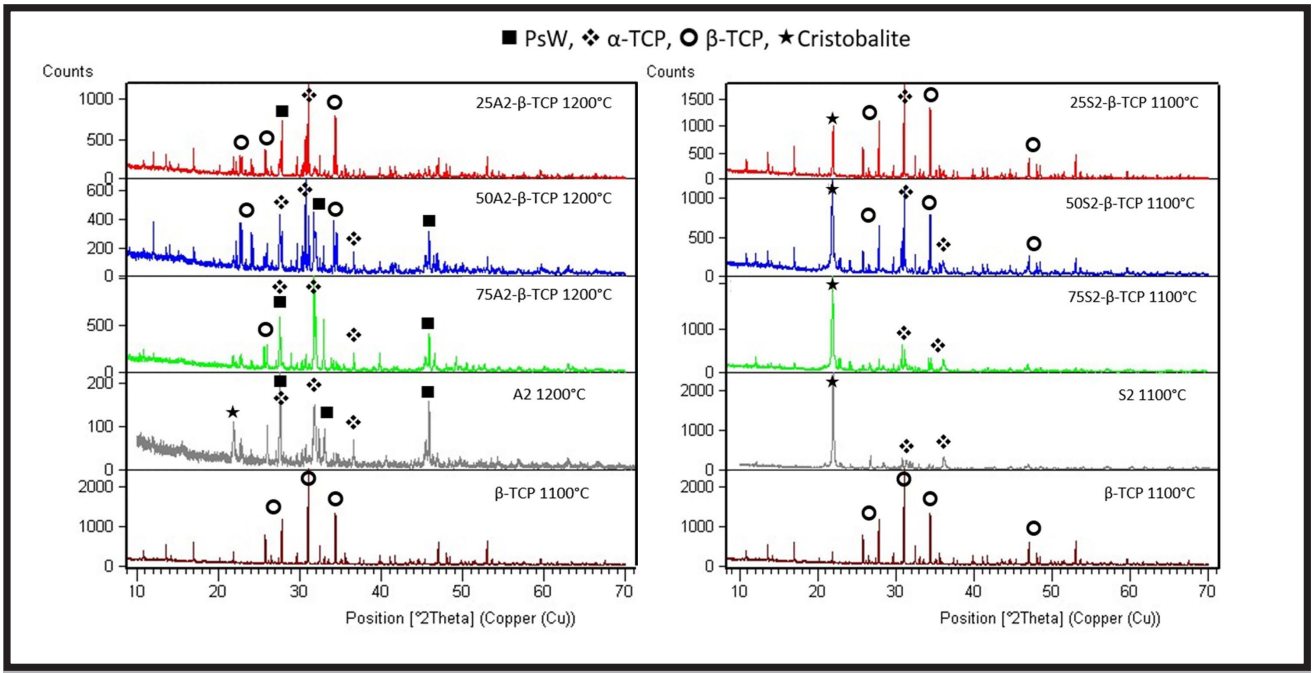

FIG. 5. XRD patterns of A2- β-TCP, S2- β-TCP composites and reference materials.

The composites with 25wt% of either S2 or A2 were homogenously sintered materials, which was also confirmed by the EDX analysis. In the case of the 50A2-β-TCP samples and the 50S2-β-TCP ones the weaker integration of glass particles in the β-TCP matrix was observed. These composites also showed the less uniform microstructure in comparison with other materials. With the increasing content of glass in the composite composition (75A2-β-TCP and 75S2-β-TCP) the more homogenous microstructure with uniformly distributed and well-integrated β-TCP particles in the glass matrix was presented. However, in the case of the 75A2-β-TCP materials the domains enriched with Si or Ca and P were reported by the EDX analysis. Nevertheless, the sintering process led to the smoothness of glass particles which were no longer distinguishable.

The XRD plots of the SBG-β-TCP composites and the reference materials sintered at 1100°C or 1200°C and then ground into powder for diffraction analysis are reported in FIG. 5. The reference samples were represented by the following phases: S2 – cristobalite (70.8%) and α-TCP (29.2%), A2 – pseudowollastonite PsW (66.9%), α-TCP (20.3%) and cristobalite (12.8%). The phase composition of β-TCP after sintering at 1100°C remained unchanged. The XRD analyses indicated that α-TCP, pseudowollastonite and β-TCP were the main phases of the A2-β-TCP composites. However, the content of each phase varied, depending on the content of A2 in the composite. Thus, the dominant phases for 25A2-β-TCP were β-TCP (62.3%) and α-TCP (27.2%), while for the 75A2-β-TCP – PsW (42.3%) and α-TCP (40.9%). The main phases for the S2-β-TCP composites were cristobalite, β-TCP and α-TCP. Similarly, as in the case of A2-β-TCP, the amount of S2 glass in the composite influenced its phase composition. The dominant phase for the 25S2-β-TCP materials were β-TCP (47.2%) and α-TCP (28.7%), while for the 75S2-β-TCP only two phases existed after sintering – cristobalite (54.5%) and α-TCP (45.5%). The results of XRD analyses indicated the strong correlation between the chemical composition of sol-gel glasses (A2 and S2) and the phase composition of the samples. It can be concluded that introduction of either A2 or S2 affected the β-TCP→α-TCP transformation, especially in the case of the 75S2-β-TCP materials. The alteration of the transition temperature of β-TCP to α-TCP by the Si presence has also been reported by other authors [41,42]. Finally, the increased content of α-TCP in the phase composition of composites can be considered as beneficial when considering the bioactive behaviour of materials.

Conclusions

In this work, we investigated the temperature behaviour, phase composition and microstructure of sol-gel bioactive glasses and β-TCP composites. The type of glass used as a composite addition strongly affected the shrinkage profile and the values of characteristic temperatures established upon hot-stage microscopy analyses. Based on these studies the sintering temperatures for the composites and the reference materials were established between the T_s and T_{sf} - between the first and second stage of densification. Thus, the composites and the reference materials were sintered as follows: 1100°C (S2, β-TCP, S2-β-TCP) and 1200°C (A2, A2-β-TCP). The SEM/EDX analyses showed the well-sintered and densified microstructure of composites. However, the 25(A2/S2)-β-TCP and the 75(A2-S2)-β-TCP materials proved acceptable homogeneity with the uniformly distributed and well-integrated both constituents. The chemical composition of sol-gel glass clearly influenced the phase composition of composites, but both A2-β-TCP and S2-β-TCP showed the presence of TCP (i.e. α-TCP and β-TCP) - the resorbable phase of high bioactivity and biocompatibility as the dominating one. In conclusion, our results indicate that both SBG-β-TCP composites may be an interesting candidates for biomaterials, however further investigations on mechanical strength, bioactivity or biological activity are needed.

Acknowledgments

This work was supported by the Ministry of Science and Higher Education, grant no 16.16.160.557. We are especially grateful for helpful commitment in HSM measurements by M.Sc. Tomasz Kawala and M.Sc. Justyna Smoleń.

References

[1] J.R. Jones, A. Clare: Bio-glasses: an introduction, Wiley, 2012.
[2] J.R. Jones, L.M. Ehrenfried, L.L. Hench: Optimising bioactive glass scaffolds for bone tissue engineering. Biomaterials 27 (2006) 964–973. doi:10.1016/J.BIOMATERIALS.2005.07.017.
[3] F. Baino, E. Fiume, M. Miola, E. Verné: Bioactive sol-gel glasses: Processing, properties, and applications. Int. J. Appl. Ceram. Technol. 15 (2018) 841–860. doi:10.1111/ijac.12873.
[4] Q.Z. Chen, I.D. Thompson, A.R. Boccaccini: 45S5 Bioglass®-derived glass-ceramic scaffolds for bone tissue engineering. Biomaterials 27 (2006) 2414–2425. doi:10.1016/j.biomaterials.2005.11.025.
[5] K. Cholewa-Kowalska, J. Kokoszka, M. Łączka, et al.: Gel--derived bioglass as a compound of hydroxyapatite composites. Biomed. Mater. 4 (2009) 055007. doi:10.1088/1748-6041/4/5/055007.
[6] D. Bellucci, A. Sola, V. Cannillo: Hydroxyapatite and tricalcium phosphate composites with bioactive glass as second phase: State of the art and current applications. J. Biomed. Mater. Res. Part A. 104 (2016) 1030–1056. doi:10.1002/jbm.a.35619.
[7] G. Georgiou, J.C. Knowles: Glass reinforced hydroxyapatite for hard tissue surgery - Part 1: mechanical properties. Biomaterials 22 (2001) 2811–2815. doi:10.1016/S0142-9612(01)00025-4.
[8] J. Pawlik, M. Ziąbka, R. Lach, M. Łączka, K. Cholewa-Kowalska: Tailoring the porosity, mechanical and bioactive properties of sol--gel bioactive glasses, hydroxyapatite and titanium dioxide porous composites. J. Mech. Behav. Biomed. Mater. 87 (2018) 40–49. doi:10.1016/J.JMBBM.2018.07.012.
[9] M. Dziadek, B. Zagrajczuk, E. Menaszek, K. Cholewa-Kowalska: A new insight into in vitro behaviour of poly(ε-caprolactone)/bioactive glass composites in biologically related fluids. J. Mater. Sci. 53 (2018) 3939–3958. doi:10.1007/s10853-017-1839-2.
[10] P. Gentile, M. Mattioli-Belmonte, V. Chiono, et al.: Bioactive glass/polymer composite scaffolds mimicking bone tissue, J. Biomed. Mater. Res. Part A. 100A (2012) 2654–2667. doi:10.1002/jbm.a.34205.
[11] J. Filipowska, J. Pawlik, K. Cholewa-Kowalska, G. Tylko, E. Pamula, L. Niedzwiedzki, et al.: Incorporation of sol-gel bioactive glass into PLGA improves mechanical properties and bioactivity of composite scaffolds and results in their osteoinductive properties. Biomed. Mater. 9 (2014). doi:10.1088/1748-6041/9/6/065001.
[12] R. Ravarian, F. Moztarzadeh, M.S. Hashjin, S.M. Rabiee, P. Khoshakhlagh, M. Tahriri: Synthesis, characterization and bioactivity investigation of bioglass/hydroxyapatite composite. Ceram. Int. 36 (2010) 291–297. doi:10.1016/J.CERAMINT.2009.09.016.
[13] S. Padilla, J. Román, S. Sánchez-Salcedo, M. Vallet-Regí: Hydroxyapatite/SiO_2-CaO-P_2O_5 glass materials: In vitro bioactivity and biocompatibility. Acta Biomater. 2 (2006) 331–342. doi:10.1016/J.ACTBIO.2006.01.006.
[14] D. Bellucci, A. Sola, A. Anesi, R. Salvatori, L. Chiarini, V. Cannillo: Bioactive glass/hydroxyapatite composites: Mechanical properties and biological evaluation. Mater. Sci. Eng. C. 51 (2015) 196–205. doi:10.1016/J.MSEC.2015.02.041.
[15] M. Bohner: Calcium orthophosphates in medicine: from ceramics to calcium phosphate cements. Injury 31(4) (2000) 37–47. http://www.ncbi.nlm.nih.gov/pubmed/11270080
[16] W. Habraken, P. Habibovic, M. Epple, M. Bohner: Calcium phosphates in biomedical applications: materials for the future? Mater. Today 19 (2016) 69–87. doi:10.1016/J.MATTOD.2015.10.008.
[17] J.B. Park: Bioceramics: properties, characterizations, and applications, Springer, 2008.
[18] P.K. Chu, X. Liu: Biomaterials fabrication and processing handbook, CRC Press/Taylor & Francis, 2008.
[19] O.P. Filho, G.P. La Torre, L.L. Hench: Effect of crystallization on apatite-layer formation of bioactive glass 45S5. J. Biomed. Mater. Res. 30 (1996) 509–514. doi:10.1002/(SICI)1097--4636(199604)30:4<509::AID-JBM9>3.0.CO;2-T.
[20] R. Xin, Q. Zhang, J. Chen, Y. Leng: Effects of porosity and crystallinity of glass ceramics on the *in vivo* bioactive response. Biomed. Mater. 3 (2008) 041001. doi:10.1088/1748-6041/3/4/041001.
[21] M. Plewinski, K. Schickle, et al.: The effect of crystallization of bioactive bioglass 45S5 on apatite formation and degradation. Dent. Mater. 29 (2013) 1256–1264. doi:10.1016/J.DENTAL.2013.09.016.
[22] H.-J. Ullrich, R.W. Cahn, P. Haasen, E.J. Kramer (Eds). Materials science and technology A comprehensive treatment. Vol. 2B: Characterization of Materials (Part II) Volume Editor: E. Lifshin. VCH Weinheim; New York; Basel; Cambridge; Tokyo 1994 doi:10.1002/crat.2170290603.
[23] S. (Severin) Amelinckx, Handbook of microscopy: applications in materials science, solid-state physics, and chemistry, VCH, 1997.
[24] A.R. Boccaccini, B. Hamann: Review In Situ high-temperature optical microscopy, J. Mater. Sci. 34 (1999) 5419–5436. doi:10.1023/A:1004706922530.
[25] H. Sholze: Influence of viscosity and surface tension on hot--stage microscopy measurements on glasses, Ber. Dtsch. Keram. Ges. 39 (1962) 63–68.
[26] M. Garcia-Valles, H.S. Hafez, I. Cruz-Matías, E. Vergés, M.H. Aly, J. Nogués, D. Ayala, S. Martínez: Calculation of viscosity–temperature curves for glass obtained from four wastewater treatment plants in Egypt, J. Therm. Anal. Calorim. 111 (2013) 107–114. doi:10.1007/s10973-012-2232-7.
[27] H. Scholze: Influence of viscosity and surface tension on hot-stage microscopy measurements on glasses. Ver. Dtsch. Keramische Gesellschaft. 391 (1962) 63–8.
[28] R.L. Dumitrache, I. Teoreanu: Melting behaviour of feldspar porcelain glazes. UPB Sci. Bull. Ser. B Chem. Mater. Sci. 68 (2006) 3–16.
[29] E. Mancuso, O.A. Bretcanu, M. Marshall, M.A. Birch, et al.: Novel bioglasses for bone tissue repair and regeneration: Effect of glass design on sintering ability, ion release and biocompatibility, Mater. Des. 129 (2017) 239–248. doi:10.1016/J.MATDES.2017.05.037.
[30] S.S. Chon, L. Piraino, S. Mokhtari, E.A. Krull, A. Coughlan, Y. Gong, et al.: Synthesis, characterization and solubility analysis of amorphous SiO_2-CaO-Na_2O-P_2O_5 scaffolds for hard tissue repair, J. Non. Cryst. Solids. 490 (2018) 1–12. doi:10.1016/j.jnoncrysol.2018.03.006.
[31] F. Baino, E. Fiume, M. Miola, F. Leone, B. Onida, F. Laviano, R. Gerbaldo, E. Verné: Fe-Doped Sol-Gel Glasses and Glass--Ceramics for Magnetic Hyperthermia. Mater. (Basel, Switzerland). 11 (2018). doi:10.3390/ma11010173.
[32] M. Araújo, M. Miola, G. Baldi, J. Perez, E. Verné: Bioactive Glasses with Low Ca/P Ratio and Enhanced Bioactivity. Mater. (Basel, Switzerland). 9 (2016). doi:10.3390/ma9040226.
[33] F. Baino, M. Ferraris, O. Bretcanu, E. Verné, C. Vitale-Brovarone: Optimization of composition, structure and mechanical strength of bioactive 3-D glass-ceramic scaffolds for bone substitution. J. Biomater. Appl. 27 (2013) 872–890. doi:10.1177/0885328211429193.
[34] A.W. Wren, A. Coughlan, K.E. Smale, S.T. Misture, B.P. Mahon, O.M. Clarkin, M.R. Towler: Fabrication of CaO–NaO–SiO_2/TiO_2 scaffolds for surgical applications, J. Mater. Sci. Mater. Med. 23 (2012) 2881–2891. doi:10.1007/s10856-012-4746-8.
[35] J. Vecstaudza, M. Gasik, J. Locs: Amorphous calcium phosphate materials: Formation, structure and thermal behaviour. J. Eur. Ceram. Soc. 39 (2019) 1642–1649. doi:10.1016/J.JEURCERAMSOC.2018.11.003.
[36] V.O. Soares, J.K.M.B. Daguano, C.B. Lombello, O.S. Bianchin, L.M.G. Gonçalves, E.D. Zanotto: New sintered wollastonite glass-ceramic for biomedical applications, Ceram. Int. 44 (2018) 20019–20027. doi:10.1016/J.CERAMINT.2018.07.275.
[37] J. Pawlik, M. Ziąbka, R. Lach, M. Łączka, K. Cholewa-Kowalska: Tailoring the porosity, mechanical and bioactive properties of sol--gel bioactive glasses, hydroxyapatite and titanium dioxide porous composites. J. Mech. Behav. Biomed. Mater. 87 (2018) 40–49. doi:10.1016/j.jmbbm.2018.07.012.
[38] J. Pawlik, M. Widziołek, K. Cholewa-Kowalska, M. Łączka, A.M. Osyczka: New sol-gel bioactive glass and titania composites with enhanced physico-chemical and biological properties. J. Biomed. Mater. Res. - Part A. 102 (2014). doi:10.1002/jbm.a.34903.
[39] M. Łączka, K. Cholewa, A. Łączka-Osyczka: Gel-derived powders of CaO-P_2O_5-SiO_2 system as a starting material to production of bioactive ceramics. J. Alloys Compd. 248 (1997) 42–51. doi:10.1016/S0925-8388(96)02648-5.
[40] M. Łączka, K. Cholewa-Kowalska, K. Kulgawczyk, M. Klisch, W. Mozgawa: Structural examinations of gel-derived materials of the CaO-P_2O_5-SiO_2 system. J. Mol. Struct. 511–512 (1999) 223–231. doi:10.1016/S0022-2860(99)00163-5.
[41] A.M. Pietak, J.W. Reid, M.J. Stott, M. Sayer: Silicon substitution in the calcium phosphate bioceramics, Biomaterials. 28 (2007) 4023–4032. doi:10.1016/J.BIOMATERIALS.2007.05.003.
[42] J. Duncan, S. Hayakawa, A. Osaka, J.F. MacDonald, J.V. Hanna, J.M.S. Skakle, I.R. Gibson: Furthering the understanding of silicate-substitution in α-tricalcium phosphate: An X-ray diffraction, X-ray fluorescence and solid-state nuclear magnetic resonance study, Acta Biomater. 10 (2014) 1443–1450. doi:10.1016/j.actbio.2013.11.014.